OJ Logo

; revised .

Space-Air-Ground Integrated Networks: Their Channel Model and Performance Analysis

CHAO ZHANG* (Member, IEEE), QINGCHAO LI* (Member, IEEE), CHAO XU* (Senior Member, IEEE), LIE-LIANG YANG* (Fellow, IEEE), AND LAJOS HANZO* (Life Fellow, IEEE)

[1]School of Electronics and Computer Science, University of Southampton, Southampton SO17 1BJ, U.K.

CORRESPONDING AUTHOR: Lajos Hanzo (e-mail: lh@ecs.soton.ac.uk).

ABSTRACT Given their extensive geographic coverage, low Earth orbit (LEO) satellites are envisioned to find their way into next-generation (6G) wireless communications. This paper explores space-air-ground integrated networks (SAGINs) leveraging LEOs to support terrestrial and non-terrestrial users. We first propose a practical satellite-ground channel model that incorporates five key aspects: 1) the small-scale fading characterized by the Shadowed-Rician distribution in terms of the Rician factor K, 2) the path loss effect of bending rays due to atmospheric refraction, 3) the molecular absorption modelled by the Beer-Lambert law, 4) the Doppler effects including the Earth's rotation, and 5) the impact of weather conditions according to the International Telecommunication Union Recommendations (ITU-R). Harnessing the proposed model, we analyze the long-term performance of the SAGIN considered. Explicitly, the closed-form expressions of both the outage probability and of the ergodic rates are derived. Additionally, the upper bounds of bit-error rates and of the Goodput are investigated. The numerical results yield the following insights: 1) The shadowing effect and the ratio between the line-of-sight and scattering components can be conveniently modelled by the factors of K and m in the proposed Shadowed-Rician small-scale fading model. 2) The atmospheric refraction has a modest effect on the path loss. 3) When calculating the transmission distance of waves, Earth's curvature and its geometric relationship with the satellites must be considered, particularly at small elevation angles. 3) High-frequency carriers suffer from substantial path loss, and 4) the Goodput metric is eminently suitable for characterizing the performance of different coding as well as modulation methods and of the estimation error of the Doppler effects.

INDEX TERMS Channel model, goodput, performance analysis, space-air-ground integrated networks

I. INTRODUCTION

THE next decade is expected to experience a proliferation of diverse wireless applications [1], [2]. Applications like navigation, underwater communication, and suburban communication demand extensive coverage to mitigate blind spots. However, terrestrial base stations (BSs) often face obstructions due to environmental factors, leading to unsatisfactory quality of service (QoS) [3]. As a potential alternative, satellites may establish line-of-sight (LoS) links with terrestrial receivers, thereby enhancing the coverage. Since Geostationary Earth Orbit satellites (GEOs) exhibit a latency approximately 100 times higher than that of Low Earth Orbit satellites (LEOs) [4], [5], LEOs are better suited for delay-sensitive communications in space-air-ground integrated networks (SAGINs).

Naturally, new applications are always accompanied by novel challenges: 1) LEOs travel in space at a velocity of around 7.8 km per second with approximately 90 minutes to complete a full circle around the Earth, resulting in a severe Doppler shift and a short serving period. 2) Electromagnetic waves must propagate through the atmosphere from the LEOs to the ground, experiencing molecular absorption, especially in the Troposphere. Below 270 GHz, the primary components responsible for molecular absorption are oxygen and water vapor. In frequency bands below 6 GHz, molecular absorption is negligible since the first significant absorption peak appears at around 22-25 GHz for water vapour. Since the L band (1-2 GHz), exploited for the current satellite-ground communications, avoids severe molecular absorption, while the bands at higher frequencies than the L band may experience high absorption peaks owing to various gases.

3) The atmospheric turbulence imposes extra shadowing effects and multi-path propagation compared to terrestrial networks, which requires suitable small-scale fading models. 4) The atmospheric refraction causes bending rays, but their length must be imposed by to obtain the exact path loss. Additionally, the path loss of high-frequency carriers is significantly severe. 5) The propagation of microwaves is influenced by the weather conditions as well, including rain, fog, and clouds.

To address these challenges, substantial research efforts have been dedicated to investigating SAGIN channel modelling and to their performance analysis, which are summarized as follows:

- **Small-scale fading**: A variety of distribution models have been considered for small-scale fading. Specifically, although the Log-Normal distribution fits the shadowing effects well [6], the Shadowed-Rician distribution [7] has mathematically-tractable expressions for fundamental channel statistics, which is widely harnessed for SAGINs [8]–[10]. Although the Shadowed-Rician distribution is generally considered to be a subtype of Rician distribution, the analytical relationships between them, particularly regarding the distribution of the Rician factor K and its properties in SAGINs, have not been fully explored yet.
- **Path loss**: Again, due to the variation of atmospheric density, the transmission path of electromagnetic waves forms a bending ray. The authors of [11], [12] have characterized the bending rays by the ray-tracing model. The additional distance caused by atmospheric refraction may lead to extra path loss, which has not been considered in current literature. Additionally, the curvature of the Earth and the geometric relationship between the satellite and terrestrial users are often overlooked in the open literature.
- **Molecular absorption**: In [13], a gas absorption model has been proposed, which requires experimentally measured absorption coefficients. A theoretical physics-based model of molecular absorption has been constructed by the Born-Oppenheimer Approximation in [14]. Based on diffusion loss, Sutherland and Bass [15] have derived absorption equations for various gases, including oxygen, nitrogen, carbon dioxide, and ozone. As a benefit of its mathematical tractability, the Beer-Lambert-law-based model has been widely exploited in Terahertz band airplane-satellite communications [16]–[18]. Despite the significant power-domain loss encountered in Terahertz band communications, the molecular absorption model exploited might serve as a viable option in the context of SAGINs.
- **Doppler effects**: Considering the geometric relationship between a terrestrial user and a satellite, a normalized maximum Doppler frequency has been derived in [19] along with its distribution in [20]. Given the normalized maximum Doppler frequency, the Doppler shift distribution has been modelled as a Jakes distribution in [21]. Further mitigation of the Doppler effects has been achieved by non-coherent detection [22] Doppler frequency shift estimation [23], and orthogonal time frequency space (OTFS) modulation [24], [25]. Nonetheless, the impact of the Earth's rotation on the relative velocity and Doppler effect has not been investigated.
- **Weather conditions**: Weather conditions also influence the propagation of electromagnetic waves, which include rain [26], [27], clouds [6], [28], and fog [28]. Specifically, the International Telecommunication Union (ITU-R) recommends methods for evaluating the attenuation due to the weather conditions in decibels (dB) [26], [28], but the attenuation in the power-domain is not directly provided.

Against this background, for the first time in literature, we propose an improved SAGIN channel model that incorporates the following practical considerations: 1) the normalized Doppler frequency along with the impact of the Earth's rotation, 2) the Beer-Lambert-law-based model of molecular absorption, 3) the Shadowed-Rician distribution in terms of the Rician factor K, 4) the path loss model considering geographic distances and bending rays, and 5) the effect of weather conditions in accordance with ITU-R's guidance. The novel contributions of this paper are contrasted to the state-of-the-art in Table 1, which are further elaborated on as follows:

- We propose a practical channel model for SAGINs, where LEOs are leveraged to directly serve SAGIN users. In this model, we consider two types of users: terrestrial and non-terrestrial users. Taking the Earth's rotation into account, we incorporate the Earth's angular velocity into the channel modelling between LEOs and terrestrial users. The Earth's rotation effect is also inherently embedded into the velocity of non-terrestrial users.
- We evaluate five key aspects of SAGIN channel modelling. Firstly, as for small-scale fading, we utilize the Shadowed-Rician channel and analyze the distribution in terms of the Rician factor K that characterizes the LoS and non-line-of-sight (nLoS) components. Secondly, as for large-scale fading, we take into account the curvature of the Earth, the geographical relationship between users and satellites, and the atmospheric refraction. The length of the bending propagation trajectory is calculated by exploiting the ray-tracing model. We then derive the "straight-line" distance between the user and the LEO as the benchmark for bending rays. We compare the satellites' true elevation angles and the detected angle of arrival for electromagnetic waves as well. Subsequently, we present the Beer-Lambert-law-based model for molecular absorption, followed by the derivation of the normalized maximum Doppler

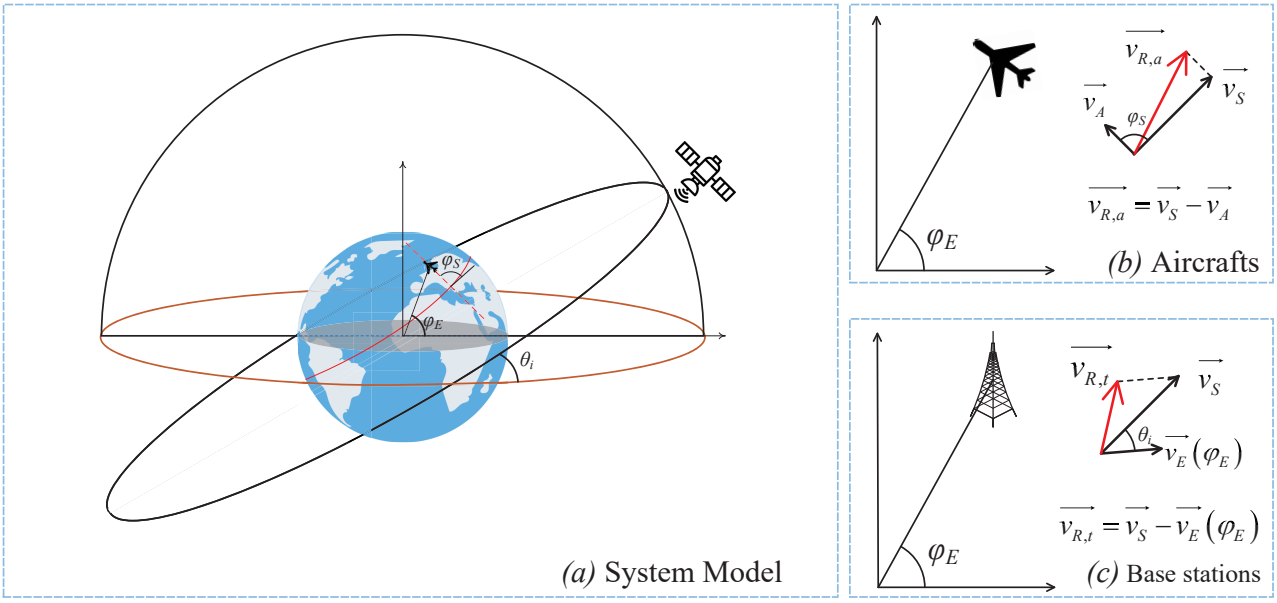

FIGURE 1. Illustration of the system model: (a) The overview of the system model, (b) Aircraft as users, and (c) Base stations or gateways as users.

frequency for both terrestrial and non-terrestrial users. Finally, we examine the effects of weather conditions in both dB and in terms of Watts (W).

- Based on the proposed SAGIN channel model, we have further quantified and analysed the following three pivotal performance metrics of SAGINs. Firstly, we calculate the achievable upper bound of bit-error-rates (BER) considering multiple quadrature amplitude modulation (M-QAM) methods. Secondly, we derive the closed-form expression of outage probability (OP), which serves as an intermediate step for calculating the ergodic rates (ER). Thirdly, we derive the Goodput (GP) attained, representing the average value of flawless reception rates that the receiver acquires over an extended duration.
- Numerical results yield the following conclusions. 1) In the proposed Shadowed-Rician small-scale fading model of SAGINs, the parameters of K and m can be appropriately adjusted to model the line-of-sight/scattering conditions and the atmospheric shadowing effect, respectively. 2) For small elevation angles, factors such as the geographic distances, geometric angles, and the curvature of the Earth should be considered for accurate path loss estimation or modelling, by contrast, they may be neglected for large elevation angles. 3) The atmospheric refraction model in ITU-R has a limited impact on path loss. 4) High-frequency carriers lead to significant path loss.

This paper is structured as follows. Section II presents a practical channel model that examines the Doppler effect, the Earth's rotation, molecular absorption, the Shadowed-Rician distribution having the Rician factor K, bending rays, the Earth's curvature, and weather conditions. Section III derives the closed-form expressions of BER, OP, ER, and GP. Section IV provides our numerical results, followed by the conclusion in Section V.

TABLE 1. The Novelty Table of the Proposed Channel Model for Space-Air-Ground Integrated Networks.

The Novelty Table								
Reference papers	Geometric Doppler frequency	Molecular absorption	Shadowed-Rician fading	The Earth's rotation	Weather conditions, inc. rain, fog, and clouds	Distribution and analysis of the Rician factors	Geometric path loss with bending rays	Goodput analysis
[19], [20]	✓			✓				
[13]–[18]		✓						
[7]–[9]			✓					
[10]			✓	✓				
[6], [26]–[28]					✓			
Our Model	✓	✓	✓	✓	✓	✓	✓	✓

II. A PRACTICAL CHANNEL MODEL

In satellite-ground communication, more severe challenges emerge than in terrestrial communication due to atmospheric interactions. Shown as Fig. 1, our SAGIN encompasses both terrestrial and non-terrestrial users communicating with a LEO. To mitigate interference, distinct sub-bands are assigned for the downlink and uplink channels. This paper is a downlink channel model. Again, in our SAGIN model, we explicitly address the following five key factors: (1) small-scale fading due to atmospheric turbulence and shadowing, (2) ray bending caused by atmospheric refractivity, (3) molecular absorption of gases, (4) the Doppler effects, and (5) weather impacts, including rain, fog, and clouds.

Theorem 1. Considering the attenuation caused by the five factors, we model the signal received at the user side as:

$$y = \sqrt{P_s \mathcal{P}_{PL} \mathcal{P}_{abs} \mathcal{P}_{Rain} \mathcal{P}_{Fog} \mathcal{P}_{Clouds}} h_{ST} x + n, \quad (1)$$

where y is the received signal, x is the transmitted signal, and n is the additive white Gaussian noise (AWGN) whose variance is expressed as σ^2. We represent the transmit power of the LEO as P_s. The parameter h_{ST} represents the small-scale fading. It obeys the Shadowed-Rician distribution, whose probability density function (PDF) and cumulative distribution function (CDF) are expressed in (7) and (8), respectively. The path loss $\mathcal{P}_{PL}$ is formulated in (21). The attenuation of molecular absorption, given by $\mathcal{P}_{abs}$, is presented in (23). The attenuation equations of fog, rain, and clouds (presented as $\mathcal{P}_{Fog}$, $\mathcal{P}_{Rain}$, and $\mathcal{P}_{Clouds}$) are encapsulated in (33) to (35), respectively, in ***Theorem* 8**.

Based on the formula of the received signal, the signal-to-noise ratio (SNR) at the user side is expressed as:

$$\gamma_{SNR} = \frac{P_s \mathcal{P}_{Loss} |h_{ST}|^2}{\sigma^2}, \quad (2)$$

where we define the long-term attenuation, formulated as $\mathcal{P}_{Loss} = \mathcal{P}_{PL} \mathcal{P}_{abs} \mathcal{P}_{Rain} \mathcal{P}_{Fog} \mathcal{P}_{Clouds}$.

Proof:
The attenuation parameters, including $\mathcal{P}_{PL}$ as the path loss, $\mathcal{P}_{abs}$ as the molecular absorption loss, and climate attenuation loss, formulated as $\mathcal{P}_{Fog}$ for fogs, $\mathcal{P}_{Rain}$ rain, and $\mathcal{P}_{Clouds}$ for clouds, are calculated in the power domain. Hence, they are placed inside the square root. Hence, the received signal is expressed as (1). The detailed derivations of each part proceed as seen in the flow chart, Fig. 2, for further clarification. ■

A. SMALL-SCALE FADING WITH SHADOWING EFFECT

The scattering effects experienced in SAGINs due to the atmosphere differ from those in terrestrial scenarios. Besides substantial reflections from buildings or walls, the primary contributors to small-scale attenuation include atmospheric turbulence, shadowing caused by gases (such as water vapour and oxygen), and weather conditions (such as fog, clouds, and rain).

1) SMALL-SCALE FADING DISTRIBUTIONS

The Log-Normal distribution may effectively represent practical scenarios [29], but this model is characterized by complex expressions, leading to intractable derivations [7]. As a more convenient alternative, the Shadowed-Rician model has gained significant popularity [8], [9]. The received complex channel information [7] is given as:

$$h_{ST}(t) = \underbrace{A(t) \exp\left[j\zeta(t)\right]}_{nLoS} + \underbrace{Z(t) \exp(j\xi)}_{LoS}, \quad (3)$$

where the scattering component, expressed as $A(t)$ is represented by a Rayleigh distribution with uniformly distributed phase $\zeta(t)$. Additionally, the line-of-sight component combined with atmospheric shadowing effects, given by $Z(t)$, is modelled as a Nakagami-m distribution with a dominant phase ξ.

Lemma 1. The PDF of the Shadowed-Rician distribution is expressed as:

$$p_{|h_{ST}|^2}(x) = \left(\frac{2b_0 m}{2b_0 m + \Omega}\right)^m \frac{1}{2b_0} \exp\left(-\frac{x}{2b_0}\right), \times {}_1F_1\left(m, 1, \frac{\Omega x}{2b_0\left(2b_0 m + \Omega\right)}\right), \quad (4)$$

where $2b_0 = \mathbb{E}[P_{nLoS}]$ is the average received power of the ground nLoS component, while $\Omega = \mathbb{E}[P_{LoS}]$ is that of the LoS component with the effect of atmospheric shadowing. The confluent hypergeometric function of the first kind is formulated as ${}_1F_1(\cdot,\cdot;\cdot)$, and m is the Nakagami-m fading parameter.

Proof:
This proof is provided in the first part of Appendix A. ■

Remark 1. Conditioned on $m = 1$, the Shadowed-Rician distribution is a Rayleigh distribution with the expectation of $(\Omega + 2b_0)$. Conditioned on $m \to \infty$, the Shadowed-Rician distribution is formulated as a Rician distribution with the Rician factor as $K_R = \frac{\Omega}{2b_0}$. The PDF expressions of the special cases are presented as:

$$p_{|h_{ST}|}(r)\Big|_{m=1} = \left(\frac{2b_0}{\Omega + 2b_0}\right) \frac{r}{b_0} \exp\left(\frac{r^2}{\Omega + 2b_0}\right), \quad (5)$$

$$p_{|h_{ST}|}(r)\Big|_{m\to\infty} = \frac{r}{b_0} \exp\left(-\frac{r^2 + \Omega}{2b_0}\right) I_0\left(\frac{\sqrt{\Omega} r}{b_0}\right). \quad (6)$$

Proof:
See the second part of Appendix A. ■

In **Lemma 1**, to calculate its CDF, the confluent hypergeometric function of the first kind, expressed as ${}_1F_1\left(m, 1, \frac{\Omega x}{2b_0(2b_0 m + \Omega)}\right)$, is difficult to formulate in integrals, especially when $m > 1$. Hence, it is desired to have a beautiful and tractable expression with meaningful parameters. Since the parameter m of the Nakagami-m distribution represents the shadowing effect of the LoS component, we define two parameters, including: 1) the shadowed LoS factor, formulated as $K_{LoS} = \frac{\Omega}{m}$, and 2)

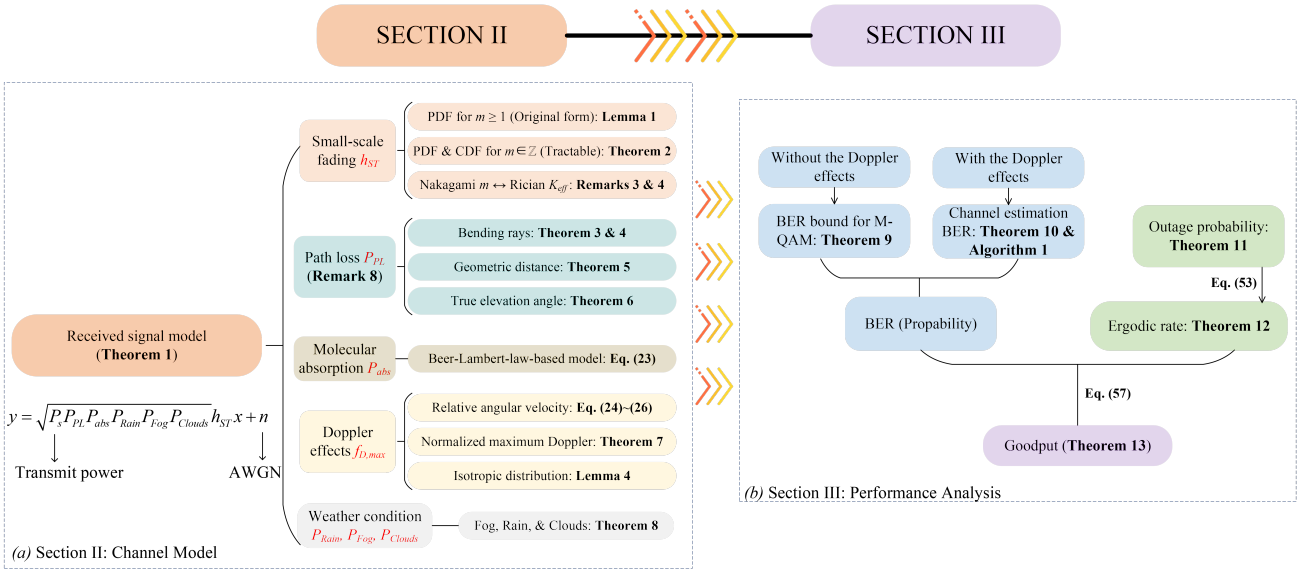

FIGURE 2. **The flow chart of this paper: (a) The channel model in Section II, and (b) the performance analysis in Section III.**

the isotropic scattering factor, expressed as $K_{Sct} = 2b_0$. In terms of physical meaning, the parameter K_{Sct} is the average received power of the nLoS components. It is also the scale parameter in the mapped exponential distribution (the square of the Rayleigh distribution). Furthermore, K_{LoS} is the scale parameter of the related Gamma distribution, which is the square of the Nakagami-m distribution.

Theorem 2. Given that m is an integer, the confluent hypergeometric function of the first kind can be transformed into a sum of exponential functions by exploiting Laguerre polynomials. When we harness the two parameters, formulated as $K_{Sct} = 2b_0$ and $K_{LoS} = \frac{\Omega}{m}$, the CDF of the Shadowed-Rician distribution of the small-scale fading model has an elegant formula, which is represented by an exponential distribution form multiplied by a binomial expansion form. Hence, the PDF and CDF expressions are formulated as:

$$f_{|h_{ST}|^2}(x) = \sum_{k=0}^{m-1} \binom{m-1}{k} \frac{(K_{Sct})^{m-k-1} (K_{LoS})^k}{k! (K_{Sct} + K_{LoS})^m} \times \left(\frac{x}{K_{Sct} + K_{LoS}} \right)^k \exp\left(-\frac{x}{K_{Sct} + K_{LoS}} \right), \quad (7)$$

$$F_{|h_{ST}|^2}(x) = 1 - \underbrace{\sum_{k=0}^{m-1} \binom{m-1}{k} \frac{(K_{Sct})^{m-k-1} (K_{LoS})^k}{(K_{Sct} + K_{LoS})^{m-1}}}_{\text{binomial expansion form}} \times \underbrace{\sum_{p=0}^{k} \frac{x^p}{p!} \left(\frac{1}{K_{Sct} + K_{LoS}} \right)^p \exp\left(-\frac{x}{K_{Sct} + K_{LoS}} \right)}_{\text{exponential distribution form}}, \quad (8)$$

where "$K_{LoS} + K_{Sct}$" represents all the components under the atmospheric shadowing effect with $K_{LoS} + K_{Sct} \leq 2b_0 + \Omega$. This clearly indicates that $K_{LoS} + K_{Sct} = 2b_0 + \Omega$ if and only if $m = 1$. Additionally, the binomial coefficient is given by $\binom{n}{k} = \frac{n!}{k!(n-k)!}$.

Proof:
See Appendix B for derivations in detail. ■

Corollary 1. By exploiting the PDF of the Shadowed-Rician fading channel, the expectation $|h_{ST}|^2$ is derived as:

$$\mathbb{E}\left[|h_{ST}|^2 \right] = 2b_0 + \Omega, \quad (9)$$

which echoes the value range of $K_{LoS} + K_{Sct}$ in **Theorem 2**.

Proof:
The proof is provided in Appendix C. ■

Remark 2. Since the transmit power, path loss, molecular absorption, and attenuation due to weather conditions are independent of each other, the small-scale fading models the multipath effect without affecting the long-term received power. Hence, we normalize the Shadowed-Rician distribution to have a unit power gain, formulated as $2b_0 + \Omega = 1$. After normalization, the PDF and CDF formulas in **Theorem 2** still hold.

2) ANALYSIS OF RICIAN FACTORS

Recall that the parameter m of the Nakagami-m distribution only represents the atmospheric shadowing effect for the LoS component. The Shadowed-Rician distribution may create the misconception that the scattering component remains unaffected by the atmospheric shadowing. Since the shadowed-Rician model represents a full-scattering scenario (isotropic reflection environment) for the nLoS components on the ground, the atmospheric shadowing effect has been

considered by adjusting m. For by the Rician channel, we characterize the ratio of the LoS component and of the scattering components due to the shadowing effect and the ground scattering by the Rician factor, formulated as:

$$K_{eff} = \frac{s^2}{2b_0 + 2\sigma_a^2}, \tag{10}$$

where s^2 is the received power of the pure LoS component, $2b_0$ is the received power of ground scattering, and $2\sigma_a^2$ is the received power of atmospheric shadowing effect.

Subsequently, we define a Rician factor to evaluate the atmospheric shadowing effect, presented as $K_{SR} = s^2/2\sigma_a^2$ subject to the constraint of $s^2 + 2\sigma_a^2 = \Omega$. Consequently, we express s^2 and $2\sigma_a^2$ by Ω, formulated as $s^2 = \frac{K_{SR}\Omega}{K_{SR}+1}$ and $2\sigma_a^2 = \frac{\Omega}{K_{SR}+1}$, respectively. Note that the relationship between the Nakagami parameter m and Rician factor K_{SR} [30] may be expressed as:

$$m = \frac{(K_{SR}+1)^2}{(2K_{SR}+1)}, \tag{11a}$$

$$K_{SR} = (m-1) + \sqrt{m^2 - m}. \tag{11b}$$

Additionally, Table 2 presents the parameters of all Rician factors, the components, and their physical meaning.

TABLE 2. Rician parameters and their physical meaning.

Parameter	Physical meaning
$K_R = \frac{\Omega}{2b_0}$	The ratio between the LoS component plus the atmospheric shadowing component and the ground scattering component
$K_{SR} = s^2/2\sigma_a^2$	The ratio between the pure LoS component and the atmospheric shadowing component
$K_{eff} = \frac{s^2}{2b_0+2\sigma_a^2}$	The ratio between the pure LoS component and all nLoS components
s^2	The received power of the pure LoS component
$2\sigma_a^2$	The received power of the atmospheric shadowing component
$s^2 + 2\sigma_a^2 = \Omega$	The received power of pure LoS component as well as the atmospheric shadowing component
$2b_0$	The received power of the ground scattering component

Remark 3. The effective Rician factor K_{eff} for the Shadowed-Rician channel is formulated as:

$$K_{eff} = \frac{\left[(m-1) + \sqrt{m^2 - m}\right]\Omega}{2b_0 + \Omega + 2b_0\left[(m-1) + \sqrt{m^2 - m}\right]}. \tag{12}$$

Remark 4. As for the shadowed LoS link, when $m = 1$, the channel conditions are extremely hostile. As m increases, the LoS link becomes more dominant, representing scenarios associated with weak atmospheric turbulence, clear skies without rain, fog, or clouds, and minimal terrestrial blockages. To echo the conclusion in **Remark 1** by exploiting K_{eff}, this remark is expressed as:

$$K_{eff}|_{m=1} = 0, \tag{13a}$$

$$K_{eff}|_{m\to\infty} = \Omega/(2b_0) = K_R, \tag{13b}$$

where we define $K_R = \Omega/(2b_0)$ is the Rician factor when there is no atmospheric fading.

B. LARGE-SCALE FADING FOR BENDING RAYS

The operational satellite communications exploit the L-band (typically 1 GHz to 2 GHz), while higher-frequency carriers, such as millimetre-wave (mm-wave) carriers, are anticipated to dominate 6G communications due to the impending spectrum crunch. Consequently, the path loss may become significant. Atmospheric refraction, which results in longer distances compared to direct LoS links, may further exacerbate this situation. This subsection aims to investigate the impact of atmospheric refraction on the path loss in 6G SAGINs.

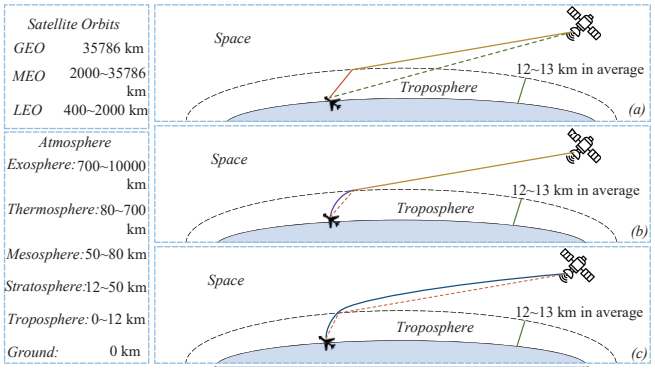

FIGURE 3. Three models of bending rays for *Theorem* 3.

In Fig. 3, three models are depicted. (1) In Fig. 3.*(a)*, a constant refractive index is assumed for both space and atmosphere, resulting in electromagnetic wave propagation mimicked by segmented broken lines. This scenario can be extended to multiple broken-line segments. (2) In Fig. 3.*(b)*, wave propagation is straight in space but follows a curved trajectory in the atmosphere. (3) In Fig. 3.*(c)*, the entire propagation path forms a continuous curve both in space and in the atmosphere.

Since the deviation of electromagnetic wave propagation is negligible in space above the atmosphere, the model in subfigure *(b)* fits practical scenarios well. Hence, it is chosen for evaluating the path loss in terms of the atmospheric refractive index formulated as $n = 1 + N \times 10^{-6}$ [11], where N denotes the radio refractivity. The radio refractivity is influenced by atmospheric pressure, water vapour pressure, absolute temperature, and a number of other factors [31]. Since horizontal variations in radio refractivity across adjacent regions are minimal, the refractive index may be modelled as a function of the vertical altitude above the Earth's surface. Based on the ITU-R recommendation sectors [31], the refractive index

as a function of the altitude is expressed as:

$$n(h) = 1 + N_0 \times 10^{-6} \times \exp\left(-\frac{h}{h_0}\right) = 1 + N_0' \exp\left(-\frac{h}{h_0}\right), \tag{14}$$

where N_0 is the average value of the atmospheric refractivity extrapolated to sea level and h_0 is the altitude within the atmosphere (km).

1) THE LENGTH OF THE BENDING PROPAGATION TRAJECTORY

Three theorems are formulated in this subsection, namely ***Theorem* 3** to ***Theorem* 5**. ***Theorem* 3** characterizes the bending trajectory of electromagnetic waves in the face of atmospheric refractivity by a ray-tracing method. Subsequently, ***Theorem* 4** extends ***Theorem* 3** with the objective of having higher accuracy. Finally, ***Theorem* 5** quantifies the straight length of the link spanning from the user to the satellite used as a benchmark.

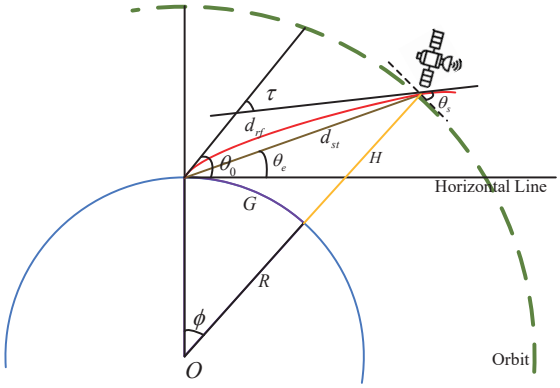

FIGURE 4. The notation of angles and distances from the satellite to the ground user for *Theorem* 3, *Theorem* 4, *Theorem* 5, and *Theorem* 6.

Before we present the following theorems, this paragraph defines parameters seen in Fig. 4 for the convenience of reading. In Fig. 4 explicitly, the blue semi-circular arc represents the Earth's surface along with its radius R represented by the black solid line. The satellite orbits around the Earth along the green dashed line, where the orbit's altitude H is indicated by the yellow solid line. The length d_{rf} of the curved trajectory from the satellite to the ground is the red curve, whose tangent at the user side forms the angle θ_0 with the horizontal line. The direct distance from the satellite to the user is d_{st}, which forms the true elevation angle θ_e with the horizontal line. The angle constituted by the tangent of the bending wave at the satellite side and that of the orbit is θ_s. The two tangents of the bending wave (the red curve) both at the user side and at the satellite side intersect, forming an angle τ. The length of the purple curve, presented as G, represents the distance along the Earth's surface, which is defined as the ground range.

***Theorem* 3.** As shown in Fig. 3.*(b)*, given the Earth's radius R, the altitude of the satellite's orbit H, and the initial (detected) elevation angle θ_0, the length of the bending path is calculated as:

$$d_{rf}(h) = \sum_{i=1}^{Q} \frac{H\omega_i n(\kappa_i)}{2}\left(1-\cos^2\left(\frac{2i-1}{2Q}\pi\right)\right)^{\frac{1}{2}} \times \left(1-\left(\frac{n_0\cos(\theta_0)}{n(\kappa_i)\left(1+\frac{\kappa_i}{R}\right)}\right)^2\right)^{-\frac{1}{2}}, \tag{15}$$

where we have $\kappa_i = \frac{H\left(\cos\left(\frac{2i-1}{2Q}\pi\right)+1\right)}{2}$, $\omega_i = \frac{\pi}{Q}$, $Q = 100$ for computing Chebyshev-Gauss quadrature. Recall that $n(\cdot)$ is shown as (14).

Proof:
This theorem is proved in Appendix D. ■

***Theorem* 4.** Based on the model shown in Fig. 4, the specific computational method given in [12] enhances the accuracy of ***Theorem* 3**, particularly in the region around the vicinity of $h = 0$ with a small θ_0. The length of the bending trajectory of electromagnetic waves may be formulated as:

$$d_{rf} = \int_0^H \frac{n^2(h)\left(1+\frac{h}{R}\right)}{\sqrt{\mu+\upsilon(h)+\omega(h)+\upsilon(h)\omega(h)}}dh = \sum_{i=1}^{Q} \frac{\omega_i H n^2(\kappa_i)\left(1+\frac{\kappa_i}{R}\right)\sqrt{1-\cos^2\left(\frac{2i-1}{2Q}\pi\right)}}{2\sqrt{\mu+\upsilon(\kappa_i)+\omega(\kappa_i)+\upsilon(\kappa_i)\omega(\kappa_i)}}, \tag{16}$$

and the ground range G is estimated by setting $\frac{h}{R}$, yielding:

$$G = \int_0^H \frac{(1+\rho_0)\cos(\theta_0)\,dh}{\left(1+\frac{h}{R}\right)\sqrt{\mu+\upsilon(h)+\omega(h)+\upsilon(h)\omega(h)}} = \sum_{i=1}^{Q} \frac{H\omega_i(1+\rho_0)\cos(\theta_0)\sqrt{1-\cos^2\left(\frac{2i-1}{2M}\pi\right)}}{2\left(1+\frac{\kappa_i}{R}\right)\sqrt{\mu+\upsilon(\kappa_i)+\omega(\kappa_i)+\upsilon(\kappa_i)\omega(\kappa_i)}}, \tag{17}$$

where the parameters and functions exploited are defined as:

$$n(x) = 1+\rho_0\exp(-kx), \tag{18a}$$
$$\mu = (1+\rho_0)^2\sin^2\theta_0 - 2\rho_0 - \rho_0^2, \tag{18b}$$
$$\upsilon(x) = 2\rho_0\exp(-kx) + \rho_0^2\exp(-2kx), \tag{18c}$$
$$\omega(x) = \frac{2x}{R} + \frac{x^2}{R^2}, \tag{18d}$$
$$\kappa_i = \frac{H\left(\cos\left(\frac{2i-1}{2Q}\pi\right)+1\right)}{2}, \tag{18e}$$
$$\omega_i = \frac{\pi}{Q}, \tag{18f}$$

with $Q = 100$ for computing Chebyshev-Gauss quadrature.

Proof:
The proof is in the first part of Appendix E. ■

Remark 5. Note that ***Theorem* 4** necessitates $\theta_0 \geq 1.5^\circ$. If we have $\theta_0 < 1.5^\circ$, negative values are obtained. This condition is satisfied in practical scenarios since LEO satellites generally work with higher elevation angles than 1.5° for the sake of better QoS (generally above 10°).

Remark 6. ***Theorem* 4** provides an adjustable refractivity function in (18a). To match the settings of the refractivity function in ITU-R and (14), we opt for fixing the value of two parameters expressed as $\rho_0 = N_0^{'}$ and $k = 1/h_0$.

Theorem 5. We harness the same parameters and geometric relationships as in ***Theorem* 4**, which are shown in Fig. 4. By extending the results in ***Theorem* 4** [11], the direct distance (the straight line d_{st}) from the satellite to the user is derived as:

$$d_{st}=\frac{(R+H)\sin\phi}{\cos\theta_e}=\sqrt{H^2+4R\,(R+H)\sin^2\left(\frac{G}{2R}\right)}, \tag{19}$$

where we have $\phi = \frac{G}{R}$ with the expression of G as (17).

Proof:
See the second part of Appendix E. ■

Remark 7. The extra length of the wave's propagation due to the atmospheric refraction is expressed as:

$$d_{\text{dif}} = d_{rf} - d_{st}. \tag{20}$$

Remark 8. The path loss is expressed as:

$$\mathcal{P}_{PL} = \left(\frac{c}{4\pi f_c}\right)^2 d_{rf}^{-\alpha_p}, \tag{21}$$

where c is the speed of light, f_c is the frequency of carrier, and α_p is the path loss exponent. To obtain the final path loss, we may exploit the results of d_{rf} in ***Theorem* 3** and ***Theorem* 4**.

Remark 9. The length of the bending signal propagation trajectory (given the d_{rf} derived in ***Theorem* 3** and ***Theorem* 4**) might be further exploited for satellite-aided integrated sensing and communications (ISaC) as well as for satellite-based cooperative localization and navigation networks.

2) THE TRUE ELEVATION ANGLE

Upon extending the results in ***Theorem* 4** and ***Theorem* 5** [12], we arrive at a computational convenient technique by calculating the true elevation angle, that is, the geometric angle of arrival (AOA), which is formulated in ***Theorem* 6**.

Theorem 6. Upon harnessing the result of G in ***Theorem* 4** and that of d_{st} in ***Theorem* 5**, the true elevation angle is expressed as:

$$\theta_e = \arcsin\left(\frac{H}{d_{st}} + \frac{H^2}{2Rd_{st}} - \frac{d_{st}}{2R}\right)\left(\theta_0 \leq \frac{\pi}{4}\right), \tag{22a}$$

$$\theta_e = \frac{\pi}{2} - \arcsin\left(\frac{(R+H)\sin\left(\frac{G}{R}\right)}{d_{st}}\right)\left(\theta_0 > \frac{\pi}{4}\right). \tag{22b}$$

Proof:
This theorem is validated by Appendix F. ■

Remark 10. The results of the true elevation angle might be exploited for investigating the effect of the polarization of antenna arrays and the LEO-aided sensing networks, including localization and navigation.

Remark 11. The elevation angle is modified by $\theta_m = (\theta_0 - \theta_e)$ radians due to the atmospheric refraction.

C. MOLECULAR ABSORPTION

When the energy of electromagnetic waves at specific frequencies matches the energy required by free electrons in molecules to be transitioned from lower to higher energy states, substantial absorption occurs. In the atmosphere, key absorbing molecules include water vapour, oxygen, nitrogen, and their isotopes. Notably, the exploitation of high-frequency bands will result in numerous molecular absorption peaks, significantly degrading wireless communication performance [18].

By combining both tractability and generality, the Beer-Lambert-law-based model has been formulated as [16], [17]:

$$\mathcal{P}_{abs}\left(f_{abs}, r_{abs}\right) = \exp\left(-\sum\nolimits_i \kappa_{abs}^i\left(f_{abs}\right) r_{abs}\right), \tag{23}$$

where the parameters include: 1) r_{abs} is the thickness of the medium, and 2) $\kappa_{abs}^i\left(f_{abs}\right)$ is the absorption coefficient of the i^{th} absorbing species (molecules or their isotopologue) at the frequency of f_{abs}. We also defined $\tau_i = \kappa_{abs}^i\left(f_{abs}\right) r_{abs}$ as the optical thickness shown in numerical results (Fig. 7). We would have a fixed r_{abs} for a homogeneous medium and a variable r_{abs} for a non-homogeneous medium [16]. The summation indicates the number of significantly impactful gases. Indicated in the simulation results, under 270 GHz, we generally only consider the effect of water vapour and oxygen.

D. THE DOPPLER EFFECT

We assume that the Earth is a perfect sphere and the orbit of the LEO is a circle concentric with the Earth. Consequently, the angular velocities of both the Earth and of the LEO remain constant over time [1]. Based on these assumptions, the relative velocity between the LEO and the terrestrial or non-terrestrial user is derived.

1) RELATIVE VELOCITY & EARTH'S ROTATION

Two categories of users are considered: airborne users (e.g., aircraft and unmanned aerial vehicles [32]) plus ground users (e.g., BSs and gateways), as illustrated in Fig. 1. *(b)* and Fig. 1. *(c)*.

As for the non-terrestrial user, the Earth's rotation influences atmospheric turbulence, leading to time-varying velocities for different eastward/westward travelling directions. We define the non-terrestrial user's velocity as $\overrightarrow{v_A}$, which

[1] We ignore the gravitation of both the moon and of other bodies in space.

inherently incorporates the effects of the Earth's rotation. Consequently, the relative velocity between the LEO and the aircraft is given by:

$$|\overrightarrow{v_{R,a}}|=|\overrightarrow{v_S}-\overrightarrow{v_A}|=\sqrt{|\overrightarrow{v_S}|^2+|\overrightarrow{v_A}|^2-2|\overrightarrow{v_S}|\,|\overrightarrow{v_A}|\cos(\varphi_S)}, \tag{24}$$

where $\overrightarrow{v_S}$ is the velocity of the LEO satellite and φ_S is the angle between the direction of $\overrightarrow{v_A}$ and that of $\overrightarrow{v_S}$.

As for the terrestrial user, the effects of the Earth's rotation must be considered. The angular velocity of the Earth is presented by ω_E, and its radius is represented by R. Let us define the angle between the user and the equatorial plane as φ_E. Furthermore, we denote the angle between the orbit and the equatorial plane as θ_i. The relative velocity between the satellite and the terrestrial user is derived as:

$$\begin{aligned}|\overrightarrow{v_{R,t}}| &= |\overrightarrow{v_S}-\overrightarrow{v_E}(\varphi_E)| \\ &= \sqrt{|\overrightarrow{v_S}|^2+R^2\omega_E^2\cos^2(\varphi_E)-2\,|\overrightarrow{v_S}|\,R\omega_E\cos(\varphi_E)\cos(\theta_i)}.\end{aligned} \tag{25}$$

Given the LEO's altitude H, the relative angular velocity is given by

$$\omega_{R,u}=\frac{|\overrightarrow{v_{R,u}}|}{R+H}, \tag{26}$$

where we have $u\in\{a,b\}$ ($u=a$ for the non-terrestrial users and $u=b$ for the terrestrial users). The formula (26) is an instantaneous relative angular velocity, which is exploited for calculating the normalized Doppler frequency, shown as (29) in the following.

2) THE DOPPLER EFFECT V.S. THE RELATIVE ANGULAR VELOCITY

Due to the Doppler effect, the observed frequency and the change of frequency are generally calculated as a function of the relative velocity, expressed as:

$$f_{ob}=\frac{c\pm v_o}{c\pm v_s}f_s\approx\left(1+\frac{\Delta v}{c}\right)f_c, \tag{27}$$

$$\Delta f=f_{ob}-f_s\approx\frac{\Delta v}{c}f_s, \tag{28}$$

where again, c is the speed of light. Furthermore, f_{ob} and v_o are the frequency and the velocity of the observer, respectively. Additionally, the frequency and the velocity of the source are respectively expressed as f_s and v_s. We have Δv as the relative velocity between the source and the target, formulated as $|v_o-v_s|$. Note that the source frequency is approximately equal to that of the carrier wave, i.e., $f_c=f_s$.

Theorem 7. When we consider both the geographic locations of users, the orbits of LEOs, and the rotation of the Earth, the Doppler effect is also influenced by the relative position between the users and the satellites [19]. Naturally, it is impossible for each user to have a satellite passing directly overhead. Explicitly, considering a maximum elevation angle between the user and the satellite is more practical. The derivation of the normalized Doppler frequency is expressed as (29), where $\omega_{R,u}$ is the relative angular velocity for the satellite, derived as (26), and θ_{max} is the maximum elevation angle. The distance from the origin of the Earth to the LEO is formulated as $H_{os}=R+H$. Additionally, we have $\dot{\psi}(t)=\frac{d\psi(t)}{dt}=\omega_{R,u}(t)$ and $\psi(t,t_0)=\psi(t)-\psi(t_0)$.

Proof:
Proved in Appendix G. ■

E. WEATHER CONDITIONS

Based on the recommendations of the ITU, the attenuation due to rain, fog, and clouds has been evaluated by considering practical data sets [26], [28]. As for the rain model, the frequencies are in the range spanning from 1 to 1000 GHz. Additionally, the attenuation model for fog and clouds is valid for frequencies below 200 GHz based on the Rayleigh scattering. The attenuation in dB is expressed in ***Lemma* 2** and the attenuation harnessed in our SNR expressions is presented in ***Theorem* 8**.

Lemma 2. The attenuation model for rain with the unit of dB/km is expressed as:

$$\gamma_R=K_R R_{rate}^{\alpha_R}, \tag{30}$$

where K_R and α_R are determined as functions of the carrier frequency, which are found in [26], while R_{rate} is the rain intensity (mm/h).

Additionally, the attenuation model for fog with the unit of dB/km is expressed as:

$$\gamma_F=K_L M_{den}, \tag{31}$$

where K_L is the specific attenuation coefficient in terms of liquid water density in the cloud or fog, expressed as M_{den} [28].

Moreover, the attenuation model for clouds with the unit of dB is expressed as:

$$\gamma_C=\frac{L_W K_L}{\sin\theta_e}, \tag{32}$$

where L_W is the statistics of the total columnar content of liquid water and θ_e is the true elevation angle [28].

Theorem 8. Instead of considering the accumulated attenuation v.s. the distance instead of in dB, we consider the attenuation as a multiplicative factor in the SNR expression.

$$f_{D,max}=\frac{\Delta f}{f_c}=-\frac{1}{c}\frac{RH_{os}\sin(\psi(t,t_0))\cos\left(\cos^{-1}\left(\frac{R\cos\theta_{\max}}{H_{os}}\right)-\theta_{\max}\right)\omega_{R,u}(t)}{\sqrt{R^2+H_{os}^2-2RH_{os}\cos(\psi(t,t_0))\cos\left(\cos^{-1}\left(\frac{R\cos\theta_{\max}}{H_{os}}\right)-\theta_{\max}\right)}}. \tag{29}$$

Hence, the specific attenuation formulas for rain, fog, and clouds are expressed as follows.

As for the rain, the attenuation model is expressed as:

$$\mathcal{P}_{Rain} = 10^{-\frac{\gamma_R d_{Rain}}{10}}, \tag{33}$$

with d_{Rain} as the length of the path that the electromagnetic waves go through in the rainfall area.

As for the fog, the attenuation model is expressed as:

$$\mathcal{P}_{Fog} = 10^{-\frac{\gamma_F d_{Fog}}{10}}, \tag{34}$$

with d_{Fog} as the length of the path that the electromagnetic waves propagate through in the foggy area.

As for the clouds, the attenuation model is expressed as:

$$\mathcal{P}_{Clouds} = \left(\prod_{i=1}^{I} 10^{\frac{\gamma_{C,i}}{10}} \right)^{-1}, \tag{35}$$

with $\gamma_{C,i}$ as the attenuation for each cloud and the number of clouds is I.

Proof:
As for the rain, we have a total attenuation due to rain, expressed as $(\gamma_R d_{Rain})$ dB. We have $\gamma_R = 10 \times \log_{10}(P_1/P_2)$, where P_1 and P_2 are the powers of waves before and after the effect of rain (per km), respectively. Hence, we have $P_{receiv} = 10^{\left(\frac{\gamma_R d_{Rain}}{10}\right)} P_{trans} = \mathcal{P}_{Rain} P_{trans}$. Consequently, the attenuation of rain, expressed as $\mathcal{P}_{Rain}$, is obtained. The attenuation expressions of other weather conditions may be similarly derived. ■

III. PERFORMANCE ANALYSIS: THE GOODPUT

Based on the practical channel model presented in the above section, in this section, the GP performance of SA-GINs is investigated. As we consider the long-term performance, we assume that the Doppler effect is averaged out. The impact of attenuation will be further evaluated by the SNR expression formulated in (2).

A. BIT-ERROR-RATE

We first provide the BER bound under QAM modulation schemes, where the Doppler effect has been well mitigated (**Theorem 9**). To evaluate the impact of the Doppler, we provide a simulation-based method to evaluate the BER under Gray coding 16-QAM by exploiting single-symbol pilot estimation to detect the signal symbols (**Theorem 10**).

1) BER BOUND

A BER bound has been evaluated in references [33]–[35] for an AWGN channel relying on M-QAM and perfect coherent phase detection:

$$\mathrm{BER_b} \leq 2 \exp\left(\frac{-3\mathbb{E}\left[\gamma_{SNR}\right]}{2\left(M-1\right)} \right), \tag{36}$$

where $\mathbb{E}\left[\cdot\right]$ is the expectation.

Under the assumption of $M \geq 4$ and $0 \leq \mathbb{E}\left[\gamma_{SNR}\right] \leq 30$ dB, we have a tighter upper bound expressed as:

$$\mathrm{BER_b} \leq \frac{1}{5} \exp\left(\frac{-3\mathbb{E}\left[\gamma_{SNR}\right]}{2\left(M-1\right)} \right). \tag{37}$$

In the following, we derive the $\mathbb{E}\left[\gamma_{SNR}\right]$ to obtain final BER bound.

Lemma 3. Recall that we normalize the expectation of $\mathbb{E}\left[\left|h_{ST}\right|^2\right]$ as $2b_0 + \Omega = 1$. Given the SNR expression in (2), we now formulate the expectation of the SNR as:

$$\mathbb{E}\left[\gamma_{SNR}\right] = \mathbb{E}\left[\lambda_t \left|h_{ST}\right|^2\right] = \lambda_t \mathbb{E}\left[\left|h_{ST}\right|^2\right] = \lambda_t, \tag{38}$$

where we have $\lambda_t = \frac{P_s P_{PL} P_{abs} P_{Rain} P_{Fog} P_{Clouds}}{\sigma^2}$.

Theorem 9. With the aid of ***Lemma* 3** and (37), the upper bound of the average long-term BER under the M-QAM is expressed as:

$$\mathrm{BER_b} \leq \frac{1}{5} \exp\left(\frac{-3\lambda_t}{2\left(M-1\right)} \right). \tag{39}$$

2) BER WITH DOPPLER EFFECTS

Since the BER bound has an assumption that the Doppler effect has been perfectly eliminated (or without the Doppler effect). Hence, the BER bound does not reflect the impact of Doppler effects. To evaluate the Doppler effect, we analyze the BER under 16-QAM, where the channel information is estimated by a pilot symbol at time t. We then detect the signal information at the later time of $t + \tau$.

Recall that the received signal is formulated as:

$$\begin{aligned} h_{ST}(t) =& A(t)\exp\left[j\zeta(t)\right] + Z(t)\exp(j\xi) \\ =& A_I(t) + jA_Q(t) + Z(t)\sin\xi + jZ(t)\cos\xi \\ =& \left(A_I(t) + Z(t)\sin\xi\right) + j\left(A_Q(t) + Z(t)\cos\xi\right), \end{aligned} \tag{40}$$

where $A_I(t)$ and $A_Q(t)$ are Gaussian random processes with zero mean and variance of b_0. Additionally, $Z(t)$ is presented as a Nakagami-m process with its parameters m and Ω.

Given a known pilot symbol s_p, the estimated channel is formulated as:

$$\hat{h}_{ST}\left(t\right) = \frac{s_p}{a_p} = h_{ST}\left(t\right) + \frac{n(t)}{a_p}, \tag{41}$$

where the average power of a symbol is denoted as $a_p^2 = P_s$.

We then exploit the estimated channel information $\hat{h}_{ST}\left(t\right)$ to detect the data symbol after time τ. Hence, the detected data symbol is expressed as:

$$\hat{x} = \frac{y}{\hat{h}_{ST}\left(t\right)} = \frac{h_{ST}\left(t+\tau\right)}{\hat{h}_{ST}\left(t\right)} x + \frac{n(t)}{\hat{h}_{ST}\left(t\right)}. \tag{42}$$

Let us now define a pair of parameters, formulated as:

$$\alpha_c = \sqrt{\bar{\gamma}}\left|h_{ST}\left(t+\tau\right)\right|, \tag{43a}$$

$$\hat{\alpha}_c = \sqrt{\bar{\gamma}}\left|\hat{h}_{ST}\left(t\right)\right|. \tag{43b}$$

Since α_c and $\hat{\alpha}_c$ are correlated within a small time slot τ, the related analytical formula may not have a closed-form expression. Hence, a simulation-based method of the correlated Shadowed-Rician random process is provided to evaluate the impact of the Doppler effect. A Shadowed-Rician random process within the time duration τ is constituted by the nLoS component (modeled by the Jakes' model) and the LoS component (a Nakagami-m random process). **Lemma 4** provides the correlated nLoS component. The correlated Nakagami-m process is evaluated by **Lemma 5**.

Lemma 4. Based on Jakes' model [21], [36], the isotropic Doppler distribution is presented as

$$p_{f_D}(f_D) = \begin{cases} \frac{1}{\pi f_{D,\max}\sqrt{1-\left(\frac{f_D}{f_{D,\max}}\right)^2}}, & |f_D| < f_{D,\max} \\ 0, & \text{else} \end{cases}, \tag{44}$$

with the aid of the Wiener-Khinchin theorem. Then, the autocorrelation of the Gaussian random processes ($A_I(t)$ and $A_Q(t)$) is expressed as:

$$R_{A_I}(\tau) = R_{A_Q}(\tau) = b_0 J_0(2\pi f_{D,max}\tau) = b_0 \rho_J(\tau), \tag{45}$$

where the parameter, formulated as $\rho_J(\tau) = J_0(2\pi f_{D,max}\tau)$, is the correlation coefficient of Gaussian random processes.

Lemma 5. It has been proved and widely exploited that a Nakagami-m distribution with its shape parameter m and its scale parameter Ω can be mimicked by $2m$ Gaussian variables, formulated as:

$$Z(t) = \sqrt{\sum_{p=1}^{2m} X_p^2(t)}, \tag{46}$$

where we have $X_p(t) \sim \mathcal{N}\left(0, \frac{\Omega}{2m}\right)$ [30]. Consequently, the Nakagami-m process is analyzed by the root of the summation of $2m$ Gaussian processes. As for each Gaussian random process, namely X_p, they have their autocorrelation, formulated as:

$$R_{X_p}(\tau) = \sqrt{\frac{\Omega}{2m}}\rho_J(\tau). \tag{47}$$

Then, we derive the autocorrelation of $Z(t)$, formulated as [37]–[39]:

$$\begin{aligned} R_Z(\tau) &= \frac{\Omega}{m}\left(\frac{\Gamma\left(m+\frac{1}{2}\right)}{\Gamma(m)}\right)^2 {}_2F_1\left(-\frac{1}{2},-\frac{1}{2};m;\rho_J^2(\tau)\right) \\ &= \Omega\rho_Z(\tau), \end{aligned} \tag{48}$$

where ${}_2F_1(\cdot,\cdot;\cdot;\cdot)$ is the hypergeometric function.

Proof:
The proof is omitted. Please see [37] for detailed derivations of the hypergeometric function. The exact formula is presented as Eq. (2) in [38]. The autocorrelation has been characterized by simulation results in Fig. 13. ■

By exploiting the conclusions in **Lemma 4** and **Lemma 5**, **Theorem 10** provides a simulation-based method for the correlated Shadowed-Rician random process.

Theorem 10. The mathematical notations in this theorem are defined as follows. Real-valued and complex-valued matrices are represented as $\mathbb{R}^{x\times y}$ and $\mathbb{C}^{k\times q}$ with k rows and q columns, respectively. $\mathcal{N}_{N\times 1}(0,q)$ represents N independent and identically distributed (i.i.d.) random Gaussian variables with a zero mean and variance q. A binary uniform distribution with N i.i.d. elements is represented as $\mathcal{U}_{N\times 1}(\{0,1\})$ for generating Gray-coded symbols. **Algorithm 1** is provided to generate the correlated Shadowed-Rician random process within a time slot τ. Then, the BER under 16-QAM is computed based on the probability function, formulated as follows:

$$\mathrm{BER_d} = \mathbb{P}\left\{\hat{x}_{MSB} > 0 \cup -2d < \hat{x}_{LSB} < 2d \,|b_1=1 \& b_2=1\right\}, \tag{49}$$

where $\mathbb{P}\{\cdot\}$ represents the probability. Additionally, $\hat{x}_{MSB}$ is the most significant bit (MSB) and $\hat{x}_{LSB}$ is the least significant bit (LSB) formulated as (42).

Verification:
Since this is a simulation-based method, it is proved by numerical results in Fig. 13 and in Fig. 14 in Section IV. ■

B. OUTAGE PROBABILITY

This subsection calculates the outage probability (OP), which is a popular performance metric also required for calculating the ergodic rates (ER). We first derive the CDF of γ_{SNR} by ***Lemma*** **6**, followed by the derivation of the OP.

Lemma 6. With the aid of the Rician distribution in ***Theorem*** **2**, the CDF expression of γ_{SNR} is derived as:

$$\begin{aligned} F_{\gamma_{SNR}}(x) =& 1 - \sum_{k=0}^{m-1}\binom{m-1}{k}\frac{(K_{Sct})^{m-k-1}(K_{LoS})^k}{(K_{Sct}+K_{LoS})^{m-1}} \\ &\times \sum_{p=0}^{k}\frac{1}{p!}\left(\frac{x}{\lambda_t(K_{Sct}+K_{LoS})}\right)^p \\ &\times \exp\left(-\frac{x}{\lambda_t(K_{Sct}+K_{LoS})}\right). \end{aligned} \tag{50}$$

Proof:
This lemma is proved by substituting the SNR expression into (8), leading to the following result:

$$F_{\gamma_{SNR}}(x) = \mathbb{P}\left\{\lambda_t|h_{ST}|^2 < x\right\} = F_{|h_{ST}|^2}\left(\frac{x}{\lambda_t}\right). \tag{51}$$

■

Theorem 11. Given the outage threshold, expressed as γ_{th}, and the derivations in ***Lemma*** **6**, the OP of this SAGIN is expressed as:

$$P_{out} = F_{\gamma_{SNR}}(\gamma_{th}) = 1 - \sum_{k=0}^{m-1}\frac{(K_{Sct})^{m-k-1}(K_{LoS})^k}{(K_{Sct}+K_{LoS})^{m-1}}$$

Algorithm 1: BER simulation-based method under the correlated Shadowed-Rician fading

Input: Maximum Doppler frequency $f_{D,max}$ in (29), time delay τ, correlation coefficient $\rho = \rho_J(\tau)$ in (47), nLoS component's power $2b_0$, Nakagami-m parameters m and Ω, numerical number N with the index idx $\in [1, \mathrm{N}]$, normalized unit bound $d = 1$ in 16-QAM constellation, and the average received SNR $\bar{\gamma} = \frac{P_s \mathcal{P}_{Loss}}{\sigma^2}$ in (2).

Output: BER.

Construct nLoS component:

$$\mathbf{A_I}(t) \sim \mathcal{N}_{N\times 1}(0, b_0) \in \mathbb{R}^{N\times 1},$$
$$\mathbf{A_Q}(t) \sim \mathcal{N}_{N\times 1}(0, b_0) \in \mathbb{R}^{N\times 1},$$
$$\mathbf{A_I}(\tau) = \rho \mathbf{A_I}(\mathbf{t}) + \sqrt{1-\rho^2}\mathcal{N}_{N\times 1}(0, b_0) \in \mathbb{R}^{N\times 1},$$
$$\mathbf{A_Q}(\tau) = \rho \mathbf{A_Q}(\mathbf{t}) + \sqrt{1-\rho^2}\mathcal{N}_{N\times 1}(0, b_0) \in \mathbb{R}^{N\times 1}.$$

Construct $2m$ Gaussian random processes:

$$\mathbf{X_p}(t) \sim \mathcal{N}_{N\times 2m}\left(0, \frac{\Omega}{2m}\right) \in \mathbb{R}^{N\times 2m},$$
$$\mathbf{X_p}(\tau) = \rho \mathbf{X_p}(\mathbf{t}) + \sqrt{1-\rho^2}\mathcal{N}_{N\times 2m}\left(0, \frac{\Omega}{2m}\right) \in \mathbb{R}^{N\times 2m}.$$

for $p \in [1, 2m]$ **do**
  Construct the Nakagami-m random process: $\mathbf{Z}(t) \in \mathbb{R}^{N\times 1}$ and $\mathbf{Z}(\tau) \in \mathbb{R}^{N\times 1}$ based on (46).
end

Construct the Shadowed-Rician random process: $\mathbf{h_{ST}}(t) \in \mathbb{C}^{N\times 1}$ and $\mathbf{h_{ST}}(\tau) \in \mathbb{C}^{N\times 1}$ based on (40).

Construct the amplitude of the Shadowed-Rician random process: $\alpha_{\mathbf{c}} = \sqrt{\bar{\gamma}}\left|\mathbf{h_{ST}}(t+\tau)\right|^2 \in \mathbb{R}^{N\times 1}$ and $\hat{\alpha}_{\mathbf{c}} = \sqrt{\bar{\gamma}}\left|\hat{\mathbf{h}}_{\mathbf{ST}}(t)\right|^2 \in \mathbb{R}^{N\times 1}$ based on (41), (43a), (43b).

Construct Gray-coded symbols:

$$\mathbf{b}_1 \sim \mathcal{U}_{N\times 1}(\{0,1\}) \in \mathbb{R}^{N\times 1}, \quad \text{for } \mathbf{x}_{\text{LSB}}$$
$$\mathbf{b}_2 \sim \mathcal{U}_{N\times 1}(\{0,1\}) \in \mathbb{R}^{N\times 1}, \quad \text{for } \mathbf{x}_{\text{MSB}}$$

for idx $\in [1, \mathrm{N}]$ **do**
  Construct Gray-coded symbols:

$$\mathbf{x}(\text{idx}) = \begin{cases} d, & \text{if } \mathbf{b_1}(\text{idx}) = 0, \mathbf{b_2}(\text{idx}) = 0 \\ 3d, & \text{if } \mathbf{b_1}(\text{idx}) = 0,\ \mathbf{b_2}(\text{idx}) = 1 \\ -3d, & \text{if } \mathbf{b_1}(\text{idx}) = 1,\ \mathbf{b_2}(\text{idx}) = 1 \\ -d, & \text{if } \mathbf{b_1}(\text{idx}) = 1,\ \mathbf{b_2}(\text{idx}) = 0 \end{cases}.$$

  Construct BER based on (49).
end

$$\times \binom{m-1}{k} \sum_{p=0}^{k} \frac{1}{p!} \left(\frac{\gamma_{th}}{\lambda_t \left(K_{Sct} + K_{LoS}\right)}\right)^p \times \exp\left(-\frac{\gamma_{th}}{\lambda_t \left(K_{Sct} + K_{LoS}\right)}\right). \tag{52}$$

C. ERGODIC RATES

There is a transformation from the OP expression to that of the ER [40], [41]. We denote the ER expression as R_{er} and express it as:

$$R_{er} = \mathbb{E}\left[\log_2\{1+\gamma_{SNR}\}\right] = \frac{1}{\ln 2}\int_0^\infty \frac{1 - P_{out}\left(\gamma_{th}\right)}{1+\gamma_{th}} d\gamma_{th}. \tag{53}$$

Then, the following theorem derives the closed-form expression of the ER.

Theorem 12. By substituting the results of ***Theorem* 11** into (53), the ER expression for our SAGIN is derived as:

$$R_{er} = \frac{1}{\ln 2}\sum_{k=0}^{m-1}\binom{m-1}{k}\frac{\left(K_{Sct}\right)^{m-k-1}\left(K_{LoS}\right)^k}{\left(K_{Sct}+K_{LoS}\right)^{m-1}} \times \left(I_3 + \sum_{p=1}^{k}\frac{\left(K_{Sct}+K_{LoS}\right)^p}{p!(\lambda_t)^p} I_4\right), \tag{54}$$

where we have:

$$R_{er}\,|_{p=0} = \frac{1}{\ln 2}\sum_{k=0}^{m-1}\binom{m-1}{k}\frac{\left(K_{Sct}\right)^{m-k-1}\left(K_{LoS}\right)^k}{\left(K_{Sct}+K_{LoS}\right)^{m-1}} I_3, \tag{55a}$$

$$R_{er}\,|_{p\geq 1} = \frac{1}{\ln 2}\sum_{k=0}^{m-1}\binom{m-1}{k} \times \sum_{p=0}^{k}\frac{\left(K_{Sct}\right)^{m-k-1}\left(K_{LoS}\right)^k I_4}{p!(\lambda_t)^p\left(K_{Sct}+K_{LoS}\right)^{m-1-p}}, \tag{55b}$$

with I_3 and I_4 formulated as:

$$I_3 = -\exp\left(\frac{1}{\lambda_t\left(K_{Sct}+K_{LoS}\right)}\right)\mathrm{Ei}\left(-\frac{1}{\lambda_t\left(K_{Sct}+K_{LoS}\right)}\right), \tag{56a}$$

$$I_4 = \Gamma\left(p+1\right)\Psi\left(p+1, p+1; \frac{1}{\lambda_t\left(K_{Sct}+K_{LoS}\right)}\right), \tag{56b}$$

where the exponential integral is formulated as $\mathrm{Ei}\left(x\right) = \int_{-\infty}^{x}\frac{\exp(t)}{t}dt$, $\Psi\left(\cdot,\cdot;\cdot\right)$ is the Tricomis confluent hypergeometric function [42], and $\Gamma(\cdot)$ is the complete Gamma function.

Proof:
This proof is provided in Appendix H. ■

D. GOODPUT

Finally, we present the GP expression with the Doppler effect, defined as:

$$R_{GP} = \left(1 - \mathrm{BER_d}\right) \times R_{er}, \tag{57}$$

and if the Doppler effect is well subtracted, we have a lower bound of GP, formulated as:

$$R_{GP} \geq \left(1 - \mathrm{BER_b}\right) \times R_{er}. \tag{58}$$

Theorem 13. Based on the results of ***Theorem* 9** and ***Theorem* 12**, we arrive at the final expression of the lower bound of GP, formulated as:

$$R_{GP} \geq \frac{1}{\ln 2}\left(1 - \frac{1}{5}\exp\left(\frac{-3\lambda_t}{2\left(M-1\right)}\right)\right)$$

$$\times \sum_{k=0}^{m-1} \binom{m-1}{k} \frac{(K_{Sct})^{m-k-1}(K_{LoS})^{k}}{(K_{Sct}+K_{LoS})^{m-1}} \times \left(I_3 + \sum_{p=1}^{k} \frac{(K_{Sct}+K_{LoS})^{p}}{p!(\lambda_t)^{p}} I_4 \right). \quad (59)$$

Proof:
This theorem is proved by substituting (39) and (54) into (58). ■

IV. NUMERICAL RESULTS

Our numerical results validate the accuracy of the analytical derivations in terms of the following settings. The radius of the Earth R is 6371.393 km. The altitude of the LEO H is 300 km. The transmit power P_s of the satellite is chosen from the range of $[30, 50]$ dBm. As for the noise, we calculate it by $\sigma^2 = -170 + 10 \times \log_{10}(BW) = -90$ dBm with $BW = 10^6$ Hz. As for the refractive index, we have $N_0 = 315$ and $h_0 = 7.5$ km based on the ITU-R standard. The satellite transmits at a detected elevation angle of $\theta_0 = 60^\circ$ using a 2 GHz carrier. As for the space transmission, we set the path loss component as $\alpha_p = 2$. Under a normalized channel with $\Omega + 2b_0 = 1$, we set the Shadowed-Rician distribution parameter to $m = 4$ and the Rician parameter to $K_R = \Omega/(2b_0) = 5$ dB. Thus, we have $K_{Sct} = \frac{1}{K_R+1} = 2b_0 = 0.2403$, $\Omega = 1 - 2b_0 = 0.7597$, and $K_{LoS} = \frac{\Omega}{m} = \frac{K_R}{m(K_R+1)} = 0.1899$. Hence, the effective Rician parameter is calculated as $K_{eff} = 2.8412$ dB. The outage threshold γ_{th} is 0.1 and the number of samples is 10^6 (Monte Carlo simulation samples) used for calculating the average performance. Note that the units of ER and GP are bits per cell per second per Hertz.

A. THE CHANNEL MODEL

Since the derivations in Section III are based on the small-scale fading model formulated in ***Theorem* 2**, we first validate the PDF and CDF in Fig. 5. We conclude that the analytical results of ***Theorem* 2** closely match the simulation results well under the condition of $m \in \mathbb{Z}$. Then, we glean further insights based on simulation results and on the formulas derived.

In Fig. 6, the relationship between the Nakagami parameter m and the effective Rician factor K is indicated. The effective Rician factor K has an upper bound at $K_{eff} = \frac{\Omega}{2b_0}$. This is because the atmospheric shadowing effect influences the Nakagami parameter m, while the ground scattering is fixed with its average power as $2b_0$. This results in a bound for $m \to \infty$. Additionally, when we have the Nakagami parameter of $m = 1$, the shadowing effect corresponding to the full scattering case, contributing to the Rician factor K going to zero.

Fig. 7 indicates the molecular absorption of impactful gases in terms of wave frequencies. The data for this figure is obtained from the website of the Earth Observation Data Group at the University of Oxford [43]. The metric of molecular absorption is the optical thickness at the zenith, denoted by $\tau = -\ln(1-A)$, where $A \in [0, 1]$ is the zenith absorption, representing the fraction of incident electromagnetic energy which is absorbed by the atmosphere at a given wavelength on a vertical path directly from the Earth's surface to space. Generally, there is significant absorption for $\tau > 1$, while the absorption is ignored for $\tau < 0.1$. In the range of $\tau \in [0.1, 1]$, it depends on the sensitivity of the system evaluated whether to consider or ignore the molecular absorption. In Fig. 7, the main gases at a frequency lower than 270 GHz are water vapour (H_2O), oxygen (O_2), ozone (O_3), and nitrous oxide (N_2O). We observed significant oxygen absorption within the frequency ranges of 53-66 GHz and at 119 GHz, while water exhibits substantial absorption between 180-187 GHz. Since water absorption (within 0-270 GHz) is generally in the range of $\tau \in [0.1, 1]$, it is desirable to carry out a

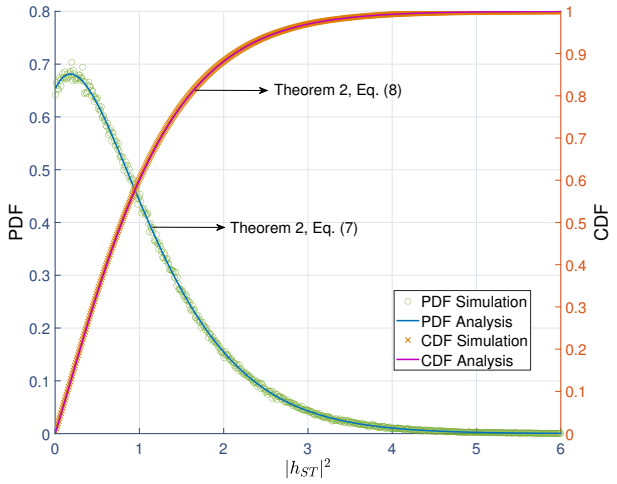

FIGURE 5. The validation of the PDF and CDF of the small-scale fading $|h_{ST}|^2$. (***Theorem* 2**)

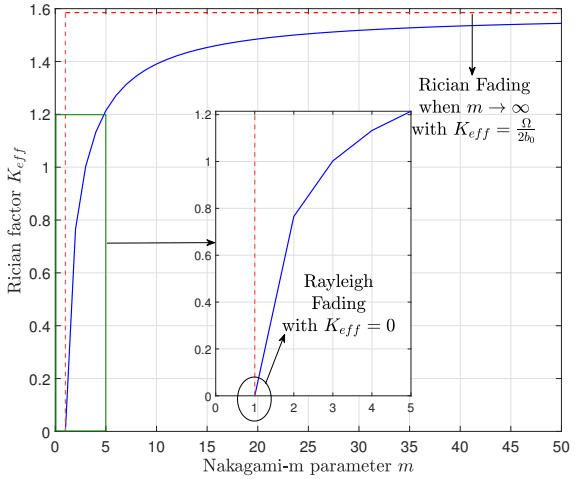

FIGURE 6. The relationship between the effective Rician factor K_{eff} and the Nakagami-m parameter m. (***Remark* 3** and ***Remark* 4**)

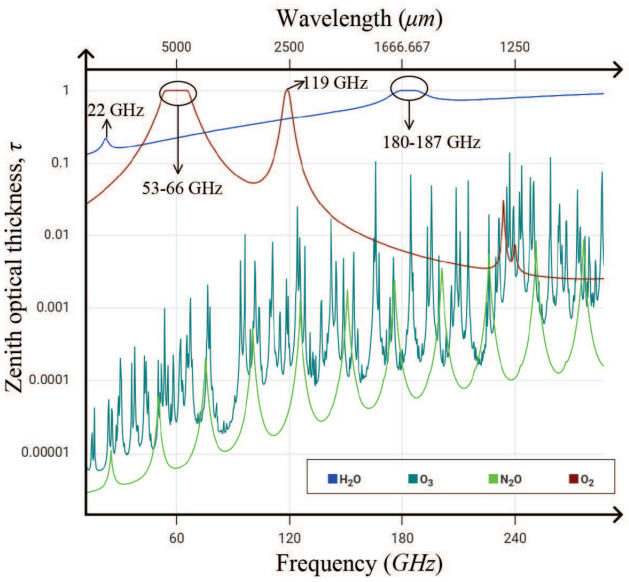

FIGURE 7. The molecular absorption in terms of frequencies for the impactful gases. (Guidance for Eq. (23))

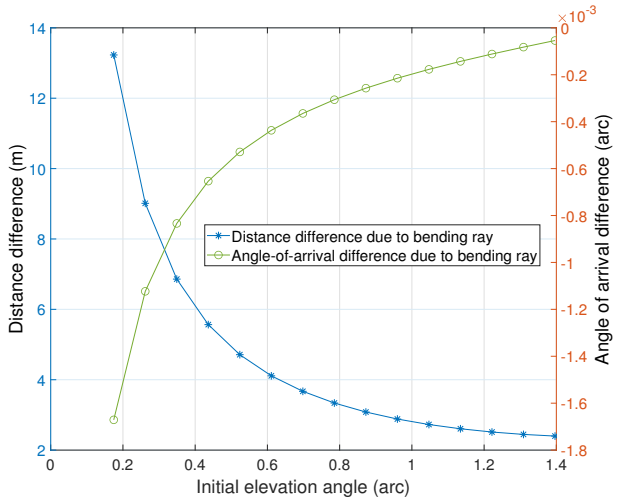

FIGURE 8. The difference between direct rays and bending rays: Distance in meters and angle in arc. (Remark 7 and Remark 11)

sensitivity test for water vapour in practical experiments in the future.

In Fig. 8, we compared the error on distance and the angle of arrival between with and without the atmospheric refractivity. The initial elevation angle range is from 10° to 80° to meet the maximum practical elevation angle range. The simulation results show that there would be an error within 2-14 meters if we do not consider the bending rays. As calculated in **Remark 11**, the difference of the angle of arrival is very limited, within $[0.1, 1.8] \times 10^{-3}$ arc. However, when exploiting the ray-tracing method to track the satellite, there would be a significant distance error (in meters), formulated as:

$$d_{diff}^{LEO} = 1000 \times 2H \sin(\theta_m/2). \tag{60}$$

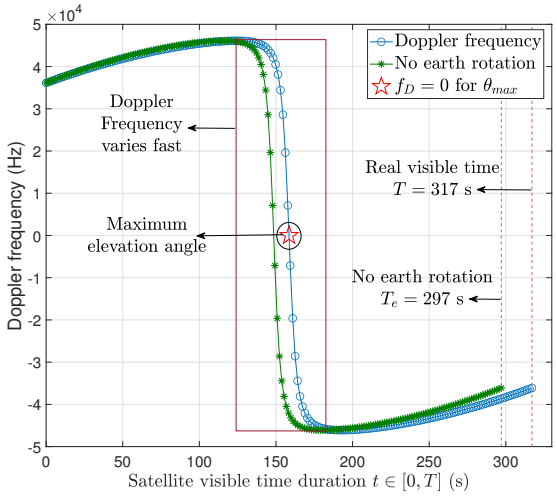

FIGURE 9. The Doppler frequency in the satellite's visible window. (Theorem 7)

With the simulation results, given $\theta_m \in [0.1, 1.8] \times 10^{-3}$ and $H = 300$ km, the calculated distance error is in the range of $d_{diff}^{LEO} \in [30, 540]$ meters.

Fig. 9 presents the unnormalized Doppler frequency v.s. time. We define the lowest elevation angle as $\theta_{in} = 10^{\circ}$. To evaluate the effect of the Earth rotation, the maximum time duration T is presented as [19]:

$$T(\theta_{\max}) \approx \frac{2}{\omega_{R,u} \cos\theta_i} \times \cos^{-1}\left(\frac{\cos\left(\cos^{-1}\left(\frac{R}{H_{os}}\cos\theta_{in}\right) - \theta_{in}\right)}{\cos\left(\cos^{-1}\left(\frac{R}{H_{os}}\cos\theta_{\max}\right) - \theta_{\max}\right)}\right), \tag{61}$$

where we have $T = 317$ s as the satellite's realistic visible window, while the time window is calculated as $T = 297$ s without the impact of the Earth rotation, which disrupted the time synchronization. In Fig. 9, it is also indicated that the Doppler frequency is zero at the largest elevation angle, where the direction of relative velocity is perpendicular to the line connecting the terrestrial user and the LEO. Additionally, in the time window from around 125 s to 175 s, the Doppler frequency varies remarkably fast. The average Doppler variation is approximately $\Delta\dot{f} = \frac{\Delta f}{\Delta t} \approx \frac{2\times4\times10^4}{175-125} = 1.6 \times 10^3$ Hz/s. During this period, sophisticated detection methods suitable for both high Doppler and large Doppler variation may be required. As for the region where Doppler varies slowly with an average variation $\Delta\dot{f} \approx \frac{1\times10^4}{325-175} = 66.7$ Hz/s, although the Doppler itself is high, the variation of the Doppler is slow. Hence, we need robust Delay-Doppler-based modulation methods to detect the signals, such as OTFS [44].

B. PERFORMANCE ANALYSIS

As for the performance metrics, including the OP, the ER, and the GP bound, we assume that the Doppler effect has

been well subtracted. We also provide simulation results of BER with the impact of the Doppler effect. Additionally, since we use a 2 GHz carrier, there is only slight molecular absorption in the L band, therefore, we ignore it. However, we would like to clarify that this model is also available to be exploited for higher-frequency bands compared to the L band, while the molecular absorption would be significant. Finally, to consider the best performance, the following simulation results are acquired under good weather conditions. The effects of rain, fog, and clouds are considered as a parameter affecting the following results.

In Fig. 10, the accuracy of the OP expression is validated versus the received SNR. Since the parameter m in the Shadowed-Rician fading channels represents the influence of the shadowing effect on the LoS component, we compare the OP as expected for different values of m. The simulation results indicate that a higher m has a lower OP. This is because increasing the parameter m leads to reduced shadowing effects according to our model.

We evaluate the path loss for the different geometric models in Fig. 11, including bending rays considering the Earth's curvature, direct line considering the Earth's curvature, and the benchmark $d = \frac{H}{\sin\theta_0}$. In some papers, to reduce the complexity of the derivation, the Earth's surface is considered to be a horizontal plane, which deviates from reality. Thus, according to our model, the distance used for path loss calculation is $d = H/\sin(\theta_0)$. As shown in the simulation results, the "horizontal" assumption is acceptable for large elevation angles, while inaccuracies are inevitable when we omit the Earth's curvature to calculate the path loss for low elevation angles. In terms of the path loss, the refractivity effect is limited when we exploit the refractive index function in ITU-R for dry air and good weather conditions. However, this does not mean that the effect of refractivity remains low for other scenarios, especially for humid climates. Additionally, as for the ray-tracing-based localization, there might be an error due to atmospheric refractivity up to 2-14 meters indicated in Fig. 8.

Fig. 12 verifies the accuracy of the ER derivation (with the unit as "bit per cell use"). We set the Rician factor between the shadowed LoS component and the ground scattering component to $K_R = 5$ & 10 dB, which contributes to the calculated effective Rician factor $K_{eff} = 2.84$ & 5.68 dB, respectively. The simulation results show that, as expected, a higher value of K_{eff} maps to improved ER performance. This is because a higher K_{eff} represents stronger LoS components, resulting in improved ER performance. We also conclude that high frequency carriers tend to degrade the performance of SAGINs. This is because the propagation paths in SAGINs are quite long, causing severe path loss. The path loss exponent is also higher when we have a higher carrier frequency, which further degrades the ER.

The simulation curves of the power-domain autocorrelations of fading channels, including the Rayleigh fading, the Nakagami-m fading, and the Shadowed-Rician fading, are

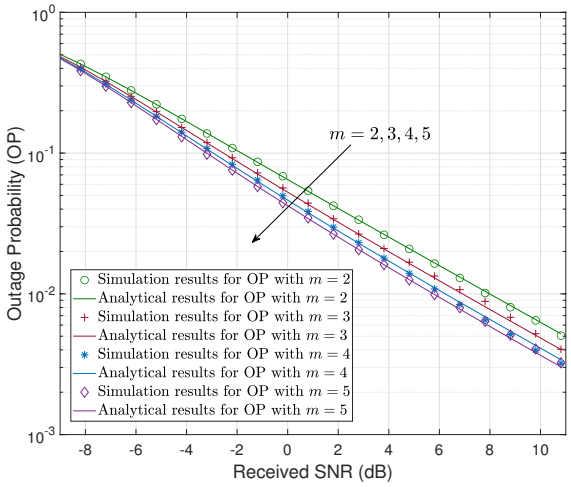

FIGURE 10. The OP versus received SNR with different $m = [2, 3, 4, 5]$ in the Shadowed-Rician fading channel (*Theorem* 2 and *Theorem* 11).

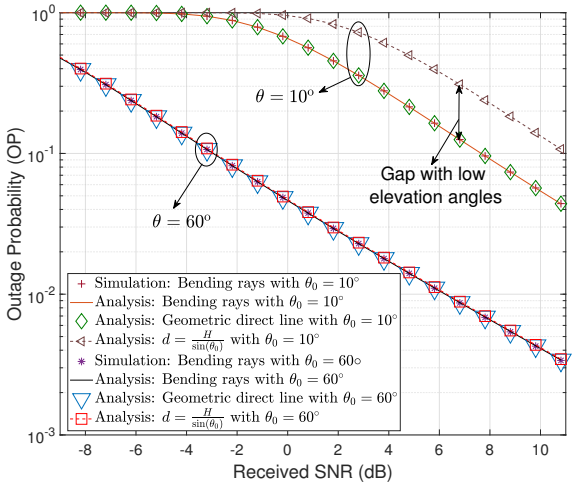

FIGURE 11. The OP versus received SNR with different elevation angles: Bending rays, direct lines, and $\frac{H}{\sin\theta_0}$ (*Theorem* 3, *Theorem* 4, *Theorem* 5 and *Theorem* 11).

indicated in Fig. 13. In terms of the time delay τ, the channel correlation of the Shadowed-Rician fading is in the middle between those of the Nakagami-m fading and the Rayleigh fading. Then, we reset the parameter K_R as 10 dB. By exploiting the channel's correlation properties, we compare the BER performance under 16-QAM between the high-SNR BER bound and the BER under correlated channels in Fig. 14. This shows that the BER performance is unsatisfactory under severe Doppler effect. Given the indicated highest Doppler frequency, $f_{D,max} \approx 4.5 \times 10^4$ Hz, it would be a disaster for signal detection if the Doppler effect is not well mitigated as seen in Fig. 9.

Given K_R as 10 dB, in Fig. 15, we analyze the relationship among the ER, the GP bound, and the GP under 16-QAM. The numerical results indicate that there is a gap between

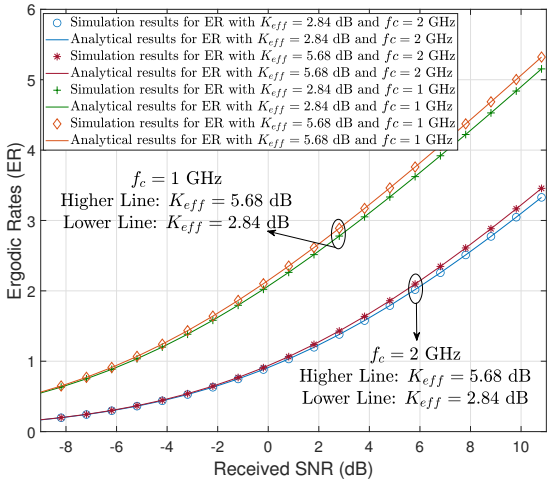

FIGURE 12. **The ER versus received SNR: the effective Rician factor K_{eff} and carrier frequency f_c (*Theorem* 12).**

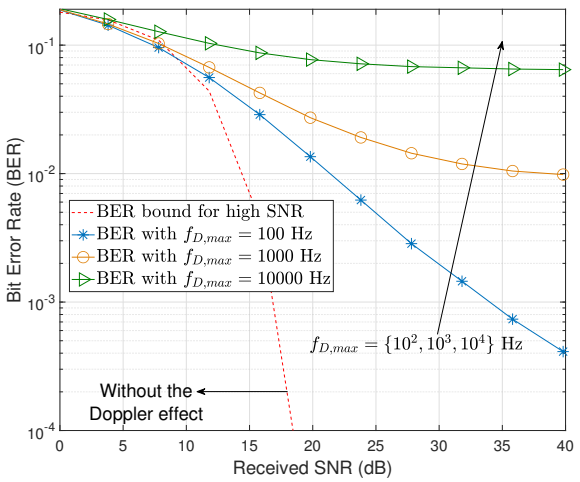

FIGURE 14. **The BER versus received SNR: The impact of Doppler effect. (*Theorem* 9 and Theorem 10).**

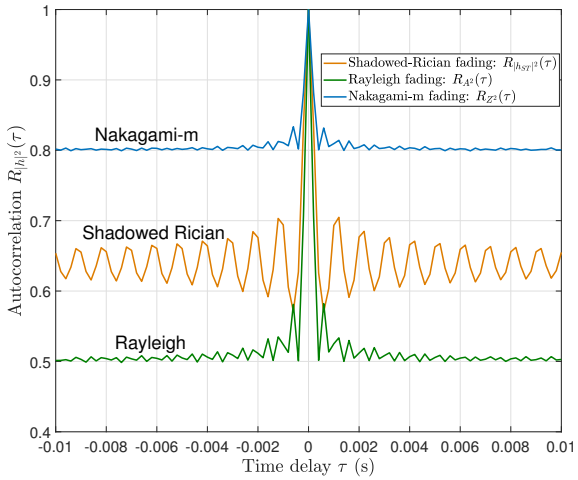

FIGURE 13. **A comparison among the autocorrelations of the Rayleigh fading, the Nakagami-m fading, and the Shadowed-Rician fading in power domain. (Lemma 4, Lemma 5, and Theorem 10)**

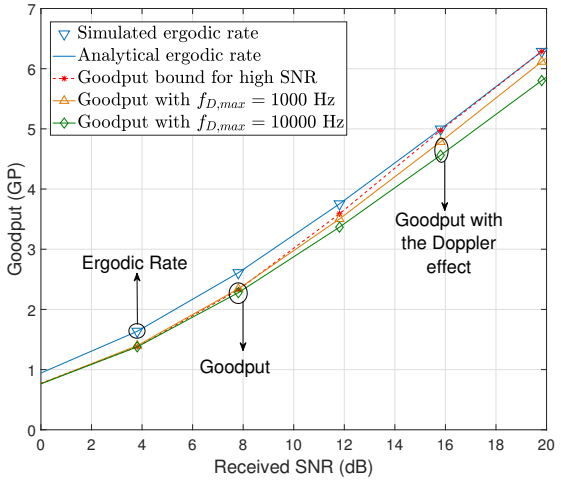

FIGURE 15. **A comparison between the ER and GP with different Doppler frequency (*Theorem* 12, and *Theorem* 13).**

the ER and GP. This is because GP has only considered the error-free throughput. Hence, the GP has the potential to evaluate the performance when we consider different coding, modulation, and channel-estimation-induced errors. For instance, when we have channel estimation errors due to the Doppler effect, the GP performance cannot even meet the lowest GP bound without estimation errors.

V. CONCLUSIONS

A practical channel model has been proposed for SAGINs, followed by an investigation of its long-term performance. The statistics of small-scale fading have been analyzed to indicate the effect of the LoS and nLoS components. The path loss along the bending rays has been calculated, and the true geometry-based elevation angle has been acquired. Furthermore, by considering the Earth's rotation, the normalized Doppler frequencies of both terrestrial and non-terrestrial users have been characterized. Also, this model has considered the effects of molecular absorption and weather conditions, like rain, fog, and clouds. By deriving the BER, OP, and ER, the upper bound of GP has been calculated for SAGINs. The impact of the Doppler effect has been investigated by the Shadowed-Rician random process. The simulation results indicate that the bending rays slightly aggravate the path loss, but influence the localization of LEO as well as the AOA. As for small elevation angles, the geometric relationship, such as the Earth's curvature, cannot be ignored. Given a large relative velocity between the LEO and a terrestrial user, the Doppler effect aggravates the BER and GP significantly. To fit the practical scenario, the GP metric conveniently lends itself to evaluating different

modulation methods, channel estimation errors, and Doppler effects.

APPENDIX A: PROOF OF LEMMA 1 and REMARK 1

1. *PROOF OF LEMMA 1*

Given the PDF of nagakami-m parameter Z as $p_Z(z) = \frac{2m^m}{\Gamma(m)\Omega^m} z^{2m-1} \exp\left(\frac{-mz^2}{\Omega}\right)$, we exploit the Rician distribution to mimic the statistic properties of the channel. Hence, the PDF of the amplitude of $|S(t)|$ is expressed as:

$$\begin{aligned} p_{|S(t)|}(r) =& \mathbb{E}_Z\left[\frac{r}{b_0}\exp\left(-\frac{r^2+Z^2}{2b_0}\right) I_0\left(\frac{Zr}{b_0}\right)\right] \\ =& \int_0^\infty \frac{r}{b_0}\exp\left(-\frac{r^2+Z^2}{2b_0}\right) I_0\left(\frac{Zr}{b_0}\right) \\ & \times \frac{2m^m}{\Gamma(m)\Omega^m} Z^{2m-1}\exp\left(\frac{-mZ^2}{\Omega}\right) dZ \\ =& \frac{2m^m}{\Gamma(m)\Omega^m}\frac{r}{b_0}\exp\left(-\frac{r^2}{2b_0}\right)\int_0^\infty Z^{2m-1} \\ & \times \exp\left(-Z^2\left(\frac{1}{2b_0}+\frac{m}{\Omega}\right)\right) I_0\left(\frac{r}{b_0}Z\right) dZ. \end{aligned} \tag{A.1}$$

Based on Eq.[6.631.1] in [45], we have the integral, expressed as:

$$\int_0^\infty x^{\nu-1} e^{-\lambda x^2} I_0(bx) dx = \frac{\Gamma(\upsilon/2)}{2\lambda^{\upsilon/2}} {}_1F_1\left(\frac{\upsilon}{2}; 1; \frac{b^2}{4\lambda}\right). \tag{A.2}$$

With the aid of the relationship of the Besell functions, expressed as $I_0(x) = J_0(ix)$, the PDF of the amplitude of the received signal is expressed as:

$$\begin{aligned} p_{|S(t)|}(r) =& \left(\frac{2b_0 m}{\Omega+2b_0 m}\right)^m \frac{r}{b_0}\exp\left(-\frac{r^2}{2b_0}\right) \\ & \times {}_1F_1\left(m; 1; \frac{\Omega r^2}{2b_0\left(\Omega+2b_0 m\right)}\right). \end{aligned} \tag{A.3}$$

In terms of the power domain, the PDF of the power of the received signal is formulated as:

$$\begin{aligned} P_{|S(t)|^2}(r) =& P_{|S(t)|}\left(\sqrt{r}\right)\frac{d\sqrt{r}}{dr} \\ =& \left(\frac{2\,b_0\,m}{\Omega+2\,b_0\,m}\right)^m \frac{1}{2\sqrt{r}\,b_0}\exp\left(-\frac{r}{2\,b_0}\right) \\ & \times {}_1F_1\left(m; 1; \frac{\Omega\, r}{2\,b_0\left(\Omega+2\,b_0\,m\right)}\right). \end{aligned} \tag{A.4}$$

2. *PROOF OF REMARK 1*

By substituting $m = 1$ and ${}_1F_1(a, a; z) = \exp(z)$ into (A.3), we formulate a Rayleigh distribution as:

$$\begin{aligned} p_{|S(t)|}(r)\Big|_{m=1} =& \frac{2r}{\Omega+2b_0}\exp\left(-\frac{r^2}{2b_0}\right) \\ & \times \exp\left(\frac{\Omega r^2}{2b_0(\Omega+2b_0)}\right) \\ =& \left(\frac{2b_0}{\Omega+2b_0}\right)\frac{r}{b_0}\exp\left(\frac{r^2}{\Omega+2b_0}\right). \end{aligned} \tag{A.5}$$

Given $m \to \infty$, we have the asymptotic expression of the confluent hypergeometric function of the first kind, formulated as:

$$\begin{aligned} {}_1F_1(a,b,x)|_{m\to\infty} =& \Gamma(b)e^{\frac{1}{2}x}\left(\left(\frac{1}{2}b-a\right)x\right)^{\frac{1}{2}-\frac{1}{2}b} \\ & \left(J_{b-1}(\sqrt{2x(b-2a)}) + \cdots\right. \\ & \left. \cdots J_{b-1}(\sqrt{2x(b-2a)})O\left(|a|^{-\frac{1}{2}}\right)\right), \end{aligned} \tag{A.6}$$

and the formula with fixed values is expressed as:

$$\begin{aligned} {}_1F_1(m,1,Kr^2)\Big|_{m\to\infty} \approx& e^{\frac{Kr^2}{2}} J_0\left(\sqrt{2Kr^2(1-2m)}\right) \\ =& e^{\frac{Kr^2}{2}} I_0\left(i\sqrt{2Kr^2(1-2m)}\right) \\ =& e^{\frac{Kr^2}{2}} I_0\left(\sqrt{2Kr^2(2m-1)}\right). \end{aligned} \tag{A.7}$$

By substituting (A.7) into (A.3), we obtain the formula as:

$$\begin{aligned} p_{|S(t|}(r) \approx& \underbrace{\left(\frac{2b_0 m}{\Omega+2b_0 m}\right)^m}_{\approx\exp\left(-\frac{\Omega}{2b_0}\right)} \frac{r}{b_0}\exp\left(-\frac{r^2}{2b_0}\right) \\ & \times \underbrace{\exp\left(\frac{\Omega r^2}{4b_0\left(\Omega+2b_0 m\right)}\right)}_{\approx\exp(0)=1} I_0\left(\frac{\sqrt{\Omega}r}{b_0}\right) \\ \approx& \frac{r}{b_0}\exp\left(-\frac{r^2+\Omega}{2b_0}\right) I_0\left(\frac{\sqrt{\Omega}r}{b_0}\right), \end{aligned} \tag{A.8}$$

where we exploit the following derivation:

$$\begin{aligned} \left(\frac{2b_0 m}{\Omega+2b_0 m}\right)^m =& \left(1-\frac{1}{m}\frac{m\Omega}{\Omega+2b_0 m}\right)^m \\ \approx& \exp\left(-\frac{m\Omega}{\Omega+2b_0 m}\right) \\ \approx& \exp\left(-\frac{\Omega}{2b_0}\right), \end{aligned} \tag{A.9}$$

where $J_x(\cdot)$ represents the Bessel function of the first kind.

APPENDIX B: PROOF OF THEOREM 2

The confluent hypergeometric function of the first kind has a special form, which is expressed as:

$$\begin{aligned} {}_1F_1\left(m; 1; c_{ST}x\right) =& \underbrace{L_{-m}\left(c_{ST}x\right)}_{\text{Laguerre polynomials}} \\ =& \exp\left(c_{ST}x\right) L_{m-1}(-c_{ST}), \end{aligned} \tag{B.1}$$

based on the definition of Laguerre polynomials associated with negative values, formulated as $L_{-n}(x) = e^x L_{n-1}(-x)$.

By further substituting the series expression of Laguerre polynomials, given by $L_n(x) = \sum_{k=0}^{n}\binom{n}{k}\frac{(-1)^k}{k!}x^k$, into the PDF of the Shadowed-Rician channel, we arrive at the final

expression of the PDF:

$$f_{|h_{ST}|^2}(x) = a_{ST} \sum_{k=0}^{m-1} \binom{m-1}{k} \frac{(c_{ST})^k}{k!} x^k \exp\left(-e_{ST}x\right), \tag{B.2}$$

where we have the parameters: $a_{ST} = \frac{1}{2b_0}\left(\frac{2b_0 m}{2b_0 m+\Omega}\right)^m$, $b_{ST} = \frac{1}{2b_0}$, $c_{ST} = \frac{\Omega}{2b_0(2b_0 m+\Omega)}$, and $e_{ST} = b_{ST} - c_{ST} = \frac{m}{2b_0 m+\Omega}$.

By exploiting the definition of the lower incomplete Gamma function, we obtain the associated CDF expression as:

$$\begin{aligned} &F_{|h_{ST}|^2}(y) \\ &= a_{ST} \sum_{k=0}^{m-1} \binom{m-1}{k} \frac{(c_{ST})^k}{k!} \int_0^y x^k \exp\left(-e_{ST}x\right) dx \\ &= a_{ST} \sum_{k=0}^{m-1} \binom{m-1}{k} \frac{(c_{ST})^k}{k! e_{ST}^{k+1}} \underbrace{\int_0^{e_{ST}y} t^{(k+1)-1} \exp\left(-t\right) dt}_{\text{Incomplete Gamma Function}} \\ &= a_{ST} \sum_{k=0}^{m-1} \binom{m-1}{k} \frac{(c_{ST})^k}{k! e_{ST}^{k+1}} \gamma\left(k+1, e_{ST}y\right). \end{aligned} \tag{B.3}$$

Note that $\Gamma(\cdot)$ is the complete Gamma function. Given a positive integer a, the lower incomplete Gamma function can be expressed by the summation of multiple exponential functions [46]–[48], formulated as:

$$\gamma(a,b) = \Gamma(a) - \Gamma(a,b) = \Gamma(a) - \sum_{p=0}^{a-1} \frac{(a-1)!}{p!} \exp(-b) b^p. \tag{B.4}$$

With the aid of the above series expansion of the complete Gamma function, the CDF expression is further expressed as:

$$\begin{aligned} F_{|h_{ST}|^2}(y) = &\underbrace{\sum_{k=0}^{m-1} \binom{m-1}{k} \varsigma(k)}_{I_1} - \sum_{k=0}^{m-1} \binom{m-1}{k} \varsigma(k) \\ &\times \sum_{p=0}^{k} \frac{(e_{ST}y)^p}{p!} \exp\left(-e_{ST}y\right), \end{aligned} \tag{B.5}$$

where we have $\varsigma(k) = a_{ST} \frac{(c_{ST})^k}{(e_{ST})^{k+1}} = \frac{(2b_0 m)^{m-k-1} \Omega^k}{(2b_0 m+\Omega)^{m-1}}$.

By exploiting the binomial expansion, the expression I_1 in (B.5) is proved to be equal to one, which is shown as follows:

$$\begin{aligned} I_1 &= a_{ST} \sum_{k=0}^{m-1} \binom{m-1}{k} \frac{(c_{ST})^k}{e_{ST}^{k+1}} \\ &= \frac{\sum_{k=0}^{m-1} \binom{m-1}{k} (2b_0 m)^{m-k-1} \Omega^k}{(2b_0 m+\Omega)^{m-1}} \\ &= \frac{(2b_0 m+\Omega)^{m-1}}{(2b_0 m+\Omega)^{m-1}} = 1. \end{aligned} \tag{B.6}$$

Consequently, the final CDF expression is derived as:

$$F_{|h_{ST}|^2}(x) = 1 - \sum_{k=0}^{m-1} \binom{m-1}{k} \sum_{p=0}^{k} \frac{\varsigma(k)}{p! (e_{ST}x)^{-p}} e^{(-e_{ST}x)}. \tag{B.7}$$

Given $K_{LoS} = \frac{\Omega}{m}$ and $K_{Sct} = 2b_0$, we have the following parameters:

$$a_{ST} = \frac{1}{K_{\text{Sct}}} \left(\frac{K_{\text{Sct}}}{K_{\text{Sct}} + K_{\text{LOS}}}\right)^m, \tag{B.8a}$$

$$b_{ST} = \frac{1}{K_{\text{Sct}}}, \tag{B.8b}$$

$$c_{ST} = \frac{K_{\text{LOS}}}{K_{\text{Sct}}(K_{\text{Sct}} + K_{\text{LOS}})}, \tag{B.8c}$$

$$\begin{aligned} e_{ST} &= \frac{m}{2b_0 m + \Omega} = \frac{1}{2b_0 + \frac{\Omega}{m}} \\ &= \frac{2b_0}{2b_0 + \Omega} + \frac{\Omega}{(2b_0 + \Omega)m} \\ &= \frac{1}{K_{Sct} + K_{LoS}}, \end{aligned} \tag{B.8d}$$

$$\begin{aligned} \zeta(k)(e_{ST})^p &= \frac{(1-K)^{m-k-1}\left(\frac{K}{m}\right)^k}{(1-K) + \frac{K}{m}^{m-1-p}} \\ &= \frac{(K_{Sct})^{m-k-1}(K_{LoS})^k}{(K_{Sct} + K_{LoS})^{m-1-p}}. \end{aligned} \tag{B.8e}$$

After substituting the parameters above into (B.2) and (B.7), the CDF and PDF are formulated as the results in ***Theorem* 2**.

APPENDIX C: PROOF OF COROLLARY 1

The expectation of $|h_{ST}|^2$ is expressed as:

$$\mathbb{E}\left[|h_{ST}|^2\right] = \int_0^\infty x f_{|h_{ST}|^2}(x) dx. \tag{C.1}$$

By substituting (B.2) into (C.1) and exploiting Eq. [2.3.4.1] of [42], we have:

$$\begin{aligned} \mathbb{E}\left[|h_{ST}|^2\right] &= a_{ST} \sum_{k=0}^{m-1} \binom{m-1}{k} \frac{(c_{ST})^k}{k!} \int_0^\infty \frac{\exp\left(-e_{ST}x\right)}{x^{-k+1}} dx \\ &= a_{ST} \sum_{k=0}^{m-1} \binom{m-1}{k} (k+1) \frac{(c_{ST})^k}{(e_{ST})^{(k+2)}}. \end{aligned} \tag{C.2}$$

By substituting the parameters a_{ST}, c_{ST}, and e_{ST} into (C.2), the targeted expectation is further derived as:

$$\mathbb{E}\left[|h_{ST}|^2\right] = \frac{2b_0 \underbrace{\sum_{k=0}^{m-1} \binom{m-1}{k} \left(\frac{\Omega}{2mb_0}\right)^k (k+1)}_{I_2}}{\left(1 + \frac{\Omega}{2b_0 m}\right)^{m-2}}. \tag{C.3}$$

We then arrive at a specific form, which is expressed as the powers of a binomial, formulated as $1 + \frac{\Omega}{2b_0 m}$, by the Binomial theorem. In the following, we express I_2 of (C.3)

as:

$$I_2=\left(1+\frac{\Omega}{2mb_0}\right)^{m-1}+(m-1)\left(\frac{\Omega}{2mb_0}\right)\left(1+\frac{\Omega}{2mb_0}\right)^{m-2}. \tag{C.4}$$

Finally, we substitute (C.4) into (C.3) to obtain the final expectation expression.

APPENDIX D: PROOF OF THEOREM 3

The differential equation of the curved trajectory's length is expressed as [12]:

$$dh/dd_{st}=\sin\left[\theta_{\beta,n}\left(h\right)\right], \tag{D.1}$$

$$dd_{rf}=n(h)dd_{st}. \tag{D.2}$$

Based on Snell's law for spherically symmetric medium [12], [49], [50], we can formulate an equation in terms of the local elevation angle, the satellite's altitude, and the refractive index, expressed as:

$$n\left(h\right)\cos\left[\theta_{\beta,n}\left(h\right)\right]\left(R+h\right)=n_0\cos\left[\theta_{\beta,n}\left(0\right)\right]R, \tag{D.3}$$

where $\theta_{\beta,n}\left(h\right)$ is the elevation angle at the location above the Earth's surface with an altitude of h.

We arrive at $n_0=n\left(0\right)=1+N_0\times10^{-6}$ upon calculating the initial atmospheric refractivity on the ground based on (14). By substituting (14) and (D.3) into (D.1), the integral expression of $d_{rf}\left(h\right)$ may be expressed as:

$$\begin{aligned}d_{rf}\left(h\right)&=\int_0^H\frac{n\left(h\right)dh}{\sin\left[\theta_{\beta,n}(h)\right]}\\&=\int_0^H\frac{n\left(h\right)dh}{\sqrt{1-\cos^2\left[\theta_{\beta,n}\left(h\right)\right]}}\\&=\int_0^H\frac{n\left(h\right)}{\sqrt{1-\left(\frac{n_0\cos(\theta_0)}{n(h)\left(1+\frac{h}{R}\right)}\right)^2}}dh.\end{aligned} \tag{D.4}$$

With the aid of the Chebyshev-Gauss quadrature shown as Eq. [25.4.38] of [51], the final expression (15) of the bending path's length is derived[2].

APPENDIX E: PROOF OF THEOREM 4 AND THEOREM 5

1. *PROOF OF THEOREM 4*

Based on the ray-tracing method, the terrestrial range is given by the following integral:

$$G=\int_0^H\frac{1}{\left(1+\frac{h}{R}\right)\sqrt{\left[\frac{n\left(1+\frac{h}{R}\right)}{n_0\cos(\theta_0)}\right]^2-1}}dh. \tag{E.1}$$

Let us define the refractivity by a general exponential function as $n=1+\rho_0\exp\left(-kh\right)$. Upon replacing $\cos^2\left(\theta_0\right)$ by the equivalent formula of $1-\sin^2\left(\theta_0\right)$, the expression of the ground range is further expressed as:

$$G=\int_0^H\frac{\left(1+\rho_0\right)\cos\left(\theta_0\right)dh}{\left(1+\frac{h}{R}\right)\sqrt{\mu+\upsilon\left(h\right)+\omega\left(h\right)+\upsilon\left(h\right)\omega\left(h\right)}}, \tag{E.2}$$

where the parameters in (E.2) are reformulated as:

$$\mu=\left(1+\rho_0\right)^2\sin^2\theta_0-2\rho_0-\rho_0^2, \tag{E.3a}$$

$$\upsilon\left(h\right)=2\rho_0\exp\left(-kh\right)+\rho_0^2\exp\left(-2kh\right), \tag{E.3b}$$

$$\omega\left(h\right)=\frac{2h}{R}+\frac{h^2}{R^2}. \tag{E.3c}$$

Subsequently, the length of the bending rays is further expressed as:

$$d_{rf}(h)=\int_0^H\frac{n^2(h)\left(1+\frac{h}{R}\right)dh}{\sqrt{\mu+\upsilon(h)+\omega(h)+\upsilon(h)\omega(h)}}, \tag{E.4}$$

where the detailed derivation is formulated in (E.5) and (E.6).

With the aid of the Chebyshev-Gauss quadrature, the closed-form expression in (E.2) is expressed as (17). Following the same derivation processes, the closed-form expression of (E.4) is formulated in (16).

2. *PROOF OF THEOREM 5*

This result is calculated by exploiting the law of cosines in the triangle constituted by the satellite, the user, and the centre of the Earth O. Given the triangle generated by the LEO, the user, and the earth centre O, we have the law of cosines equation, formulated as:

$$d_{st}^2=R^2+(R+H)^2-2R(R+H)\cos\phi. \tag{E.7}$$

With the aid of the tangent half-angle formula and $\phi=\frac{G}{R}$, we have:

$$d_{st}^2=R^2+(R+H)^2-2R(R+H)\left[1-2\sin^2\left(\frac{G}{2R}\right)\right]. \tag{E.8}$$

By exploiting that $\sin\left(\frac{\pi}{2}+\theta_e\right)=\cos\theta_e$ and substituting (17) into (19), we obtain the final result.

APPENDIX F: PROOF OF THEOREM 6

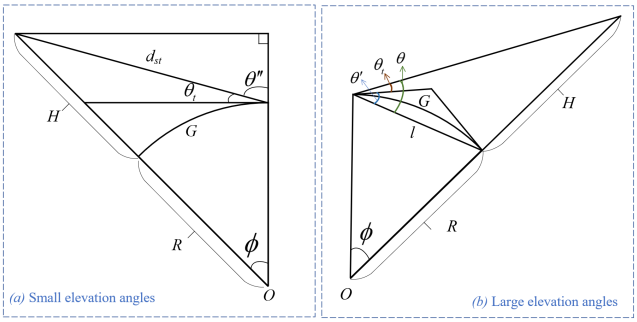

FIGURE 16. The geometric figure for calculating elevation angles.

The elevation angle evaluated under the condition of $\theta_0\leq\pi/4$ is based on the small-angle approximation. Given

[2]The definition of the Chebyshev-Gauss quadrature is expressed as $\int_{-1}^{+1}\frac{f(x)}{\sqrt{1-x^2}}dx\approx\sum_{i=1}^{n}w_if\left(x_i\right)$ where we have $x_i=\cos\left(\frac{2i-1}{2n}\pi\right)$ and the weight $w_i=\frac{\pi}{n}$.

Fig.16.*(a)* relying on the small-angle approximation, we have:

$$\sin\theta_t = \sin(\theta - \theta') = \theta - \theta' = \sin\theta - \sin\theta'. \tag{F.1}$$

Conditioned on $H \ll R$, we have a very small ϕ resulting in a assumption that the chord length l and arc length G corresponding to ϕ are approximately equal. Given $G = \phi/R$ and $G \approx \sqrt{d_{st}^2 - H^2}$, we have the following formula as:

$$\begin{aligned}\phi = \frac{G}{R} \approx \frac{\sqrt{d_{st}^2 - H^2}}{R} \overset{H\ll R}{\approx} \frac{d_{st}}{R} \overset{\phi=\frac{d_{st}}{R}}{=} \frac{(\phi R)^2}{R d_{st}} \\ \overset{G=\frac{\phi}{R}}{=} \frac{G^2}{R d_{st}} \overset{G\approx l}{\approx} \frac{l^2}{R d_{st}} = \frac{d_{st}^2 - H^2}{R d_{st}} = \frac{d_{st}}{R} - \frac{H^2}{R d_{st}}.\end{aligned} \tag{F.2}$$

Based on the tangent chord angle theorem in a circle, we have $\theta' = \phi/2$. Then, the value of $\sin\theta'$ is approximately formulated:

$$\sin\theta' \approx \theta' = \frac{\phi}{2} = \frac{d_{st}}{2R} - \frac{H^2}{2R d_{st}}, \tag{F.3}$$

and the value of $\sin\theta_t$ is formulated as:

$$\sin\theta_t = \sin\theta - \sin\theta' = \frac{H}{d_{st}} - \frac{d_{st}}{2R} + \frac{H^2}{2R d_{st}}. \tag{F.4}$$

Finally, we have $\arcsin sin\theta_t$ as the elevation angle for small angles.

As for the case of large elevation angles, based on the triangle seen in Fig.16.*(b)*, it is expressed by the law of sines as:

$$\frac{d_{st}}{\sin\phi} = \frac{R + H}{\sin(\pi - \theta'')}. \tag{F.5}$$

Given $H \ll R$, the elevation angle is formulated as:

$$\begin{aligned}\theta_t =& \frac{\pi}{2} - \theta'' = \frac{\pi}{2} - \arcsin\left[\frac{(R+H)\sin\phi}{d_{st}}\right] \\ =& \frac{\pi}{2} - \arcsin\left[\frac{(R+H)\sin\left(\frac{G}{R}\right)}{d_{st}}\right].\end{aligned} \tag{F.6}$$

APPENDIX G: PROOF OF THEOREM 7

The geometric relationship between the position of the satellite and that of the user is given in Fig. 17. Given the maximum elevation angle θ_{max}, the slant range $s(t)$ is given by the law of cosines, formulated as:

$$s(t) = \sqrt{R^2 + H_{os}^2 - 2RH_{os}\cos\gamma(t)}, \tag{G.1}$$

where $\gamma(t)$ is the angle at time t generated by the origin of the Earth, the position of the satellite at time instant t_0, and that at time t.

The spherical law of cosines is exploited, which is expressed as $\cos c = \cos a \cos b + \sin a \sin b \cos C$. Since the angle $\angle PMN$ equals $\pi/2$, we have an angular relationship expressed as:

$$\cos\gamma(t) = \cos\left(\psi(t) - \psi(t_0)\right)\cos\gamma(t_0), \tag{G.2}$$

where $\psi(t) - \psi(t_0)$, $\gamma(t_0)$, and $\gamma(t)$ are the angles constituted by the origin of the Earth and the related arc along the surface of the Earth, which is shown in Fig. 17. *(c)*.

By substituting (G.2) into (G.1) and differentiating (G.1) with respect to time t, we have:

$$\dot{s}(t) = \frac{ds(t)}{dt}$$

$$\begin{aligned}d_{rf}(h) &= \int_0^H \frac{n(h)\,dh}{\sqrt{1 - \cos^2\left[\theta_{\beta,n}(h)\right]}} \\ &= \int_0^H \frac{n(h)}{\sqrt{1 - \left(\frac{n_0\cos(\theta_0)}{n(h)\left(1+\frac{h}{R}\right)}\right)^2}} = \int_0^H \frac{[n(h)]^2\left(1+\frac{h}{R}\right)}{\sqrt{[1+\rho_0\exp(-kx)]^2\left(1+\frac{h}{R}\right)^2 - (1+\rho_0)^2\cos^2(\theta_0)}}\,dh \\ &= \int_0^H \frac{[n(h)]^2\left(1+\frac{h}{R}\right)}{\sqrt{\left\{1 + 2\rho_0\exp(-kx) + [\rho_0\exp(-kx)]^2\right\}\left[1 + \frac{2h}{R} + \left(\frac{h}{R}\right)^2\right] - (1+\rho_0)^2\cos^2(\theta_0)}}\,dh \\ &= \int_0^H \frac{[n(h)]^2\left(1+\frac{h}{R}\right)}{\sqrt{X_{term}}}\,dh,\end{aligned} \tag{E.5}$$

$$\begin{aligned}X_{term} = &\underbrace{\left\{2\rho_0\exp(-kx) + [\rho_0\exp(-kx)]^2\right\}}_{\nu(x)}\underbrace{\left[\frac{2h}{R} + \left(\frac{h}{R}\right)^2\right]}_{\omega(x)} + \underbrace{\left\{2\rho_0\exp(-kx) + [\rho_0\exp(-kx)]^2\right\}}_{\nu(x)} \\ &+ \underbrace{\left[\frac{2h}{R} + \left(\frac{h}{R}\right)^2\right]}_{\omega(x)} + \underbrace{(1+\rho_0)\sin^2(\theta_0) - 2\rho_0 - (\rho_0)^2}_{\mu}.\end{aligned} \tag{E.6}$$

$$= \frac{RH_{os}\cos\gamma(t_0)\sin(\psi(t)-\psi(t_0))\frac{d\psi(t)}{dt}}{\sqrt{R^2+H_{os}^2-2RH_{os}\cos(\psi(t)-\psi(t_0))\cos\gamma(t_0)}}$$
$$= \frac{RH_{os}\cos\gamma(t_0)\sin(\psi(t)-\psi(t_0))\dot{\psi}(t)}{\sqrt{R^2+H_{os}^2-2RH_{os}\cos(\psi(t)-\psi(t_0))\cos\gamma(t_0)}}, \tag{G.3}$$

where we define the differential equation versus time as $\dot{f}(t) = df(t)/dt$.

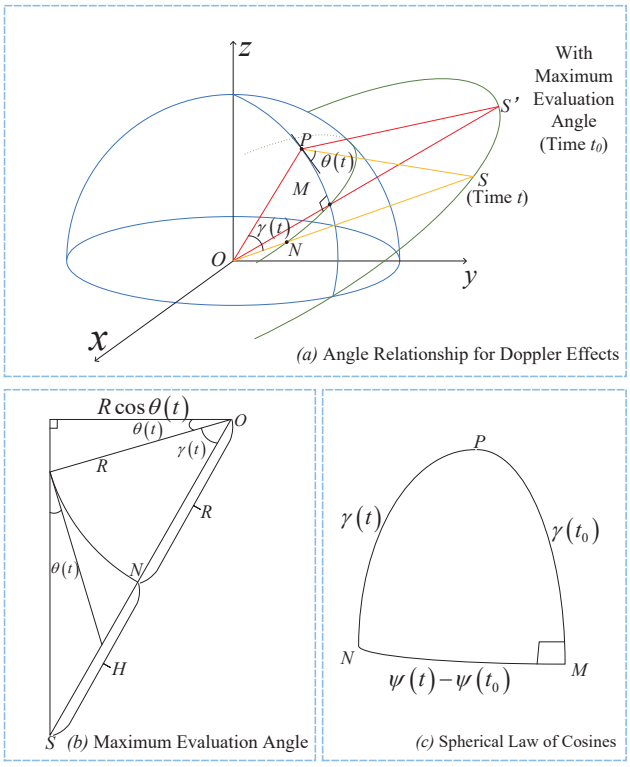

FIGURE 17. The notation of angles from the satellite to the ground user for *Theorem* 7.

We assume that at the time instant t_0, the position of the satellite is at the point of the maximum elevation angle θ_{max}, expressed as $\theta_0 = \theta_{max}$. Hence, based on the associated triangle seen in Fig. 17. *(b)*, the angle relationship satisfies:

$$\cos(\theta_{\max} + \gamma(t_0)) = \frac{R\cos\theta_{\max}}{H_{os}}, \tag{G.4}$$

where $H_{os} = R + H$ represents the straight distance from the origin of the Earth to the satellite.

By substituting (G.4) into (G.3), we arrive at the normalized Doppler frequency in terms of the maximum elevation and time t as seen in (G.5), where we have $\psi(t, t_0) = \psi(t) - \psi(t_0)$.

By considering the relative angular velocity shown as (26) in Section II, we have the final expression in this theorem.

APPENDIX H: PROOF OF THEOREM 12

Based on (53), the ergodic rate is formulated as:

$$R_{er} = \frac{1}{\ln 2}\int_0^\infty \frac{1-P_{out}(\gamma_{th})}{1+\gamma_{th}}d\gamma_{th}$$
$$= \frac{1}{\ln 2}\sum_{k=0}^{m-1}\binom{m-1}{k}\sum_{p=0}^{k}\frac{(K_{Sct})^{m-k-1}(K_{LoS})^k}{p!(\lambda_t)^p(K_{Sct}+K_{LoS})^{m-1-p}}$$
$$\times\int_0^\infty \frac{\gamma_{th}^p}{1+\gamma_{th}}\exp\left(-\frac{\gamma_{th}}{\lambda_t(K_{Sct}+K_{LoS})}\right)d\gamma_{th}. \tag{H.1}$$

Since the value of p varies in the above equation, the integral formula is split into two types of integrals based on reference [42]. As for $p = 0$, we exploit Eq. [2.3.4.3] of [42] to derive I_3, as follows:

$$R_{er}\Big|_{p=0} =$$
$$\frac{1}{\ln 2}\sum_{k=0}^{m-1}\binom{m-1}{k}\frac{(K_{Sct})^{m-k-1}(K_{LoS})^k}{(K_{Sct}+K_{LoS})^{m-1}}$$
$$\times\int_0^\infty \frac{\exp\left(-\frac{x}{\lambda_t(K_{Sct}+K_{LoS})}\right)}{1+x}dx$$
$$= \frac{1}{\ln 2}\sum_{k=0}^{m-1}\binom{m-1}{k}\frac{(K_{Sct})^{m-k-1}(K_{LoS})^k}{(K_{Sct}+K_{LoS})^{m-1}}$$
$$\times\int_0^\infty \frac{\exp\left(-\frac{x}{\lambda_t(K_{Sct}+K_{LoS})}\right)}{1+x}dx$$
$$= \frac{1}{\ln 2}\sum_{k=0}^{m-1}\binom{m-1}{k}\frac{(-1)(K_{Sct})^{m-k-1}(K_{LoS})^k}{(K_{Sct}+K_{LoS})^{m-1}}$$
$$\times\exp\left(\frac{1}{\lambda_t(K_{Sct}+K_{LoS})}\right)\mathrm{Ei}\left(-\frac{1}{\lambda_t(K_{Sct}+K_{LoS})}\right)$$
$$= \frac{1}{\ln 2}\sum_{k=0}^{m-1}\binom{m-1}{k}\frac{(K_{Sct})^{m-k-1}(K_{LoS})^k}{(K_{Sct}+K_{LoS})^{m-1}}I_3. \tag{H.2}$$

As for $p \geq 1$, Eq. [2.3.6.9] of [42] is harnessed to calculate I_4, expressed as:

$$R_{er}\Big|_{p\geq 1} =$$

$$\frac{\Delta f}{f_c} = -\frac{\dot{s}(t)}{c} = -\frac{1}{c}\frac{RH_{os}\cos\gamma(t_0)\sin(\psi(t)-\psi(t_0))\dot{\psi}(t)}{\sqrt{R^2+H_{os}^2-2RH_{os}\cos(\psi(t)-\psi(t_0))\cos\gamma(t_0)}}$$
$$= -\frac{1}{c}\frac{RH_{os}\sin(\psi(t,t_0))\cos\left(\cos^{-1}\left(\frac{R\cos\theta_{\max}}{H_{os}}\right)-\theta_{\max}\right)\dot{\psi}(t)}{\sqrt{R^2+H_{os}^2-2RH_{os}\cos(\psi(t,t_0))\cos\left(\cos^{-1}\left(\frac{R\cos\theta_{\max}}{H_{os}}\right)-\theta_{\max}\right)}}. \tag{G.5}$$

$$\frac{1}{\ln 2}\sum_{k=0}^{m-1}\binom{m-1}{k}\sum_{p=0}^{k}\frac{(K_{Sct})^{m-k-1}(K_{LoS})^{k}}{p!(\lambda_t)^{p}(K_{Sct}+K_{LoS})^{m-1-p}}$$
$$\times\int_0^{\infty}\frac{x^{p}}{1+x}\exp\left(-\frac{1}{\lambda_t(K_{Sct}+K_{LoS})}x\right)dx$$
$$=\frac{1}{\ln 2}\sum_{k=0}^{m-1}\binom{m-1}{k}\sum_{p=1}^{k}\frac{(K_{Sct})^{m-k-1}(K_{LoS})^{k}}{p!(\lambda_t)^{p}(K_{Sct}+K_{LoS})^{m-1-p}}I_4, \tag{H.3}$$

where I_4 is formulated as:

$$I_4=\int_0^{\infty}\frac{x^{(p+1)-1}}{1+x}\exp\left(-\frac{x}{\lambda_t(K_{Sct}+K_{LoS})}\right)dx$$
$$=\Gamma(p+1)\Psi\left(p+1,p+1;\frac{1}{\lambda_t(K_{Sct}+K_{LoS})}\right). \tag{H.4}$$

Finally, we combine the above results to obtain the final form as (54).

REFERENCES

[1] X. Zhu and C. Jiang, "Creating efficient integrated satellite-terrestrial networks in the 6G era," *IEEE Wireless Commun.*, vol. 29, no. 4, pp. 154–160, Aug. 2022.

[2] C. Xu, N. Ishikawa, R. Rajashekar, S. Sugiura, R. G. Maunder, Z. Wang, L.-L. Yang, and L. Hanzo, "Sixty years of coherent versus non-coherent tradeoffs and the road from 5G to wireless futures," *IEEE Access*, vol. 7, pp. 178 246–178 299, 2019.

[3] J. Liu, Y. Shi, Z. M. Fadlullah, and N. Kato, "Space-air-ground integrated network: A survey," *IEEE Commun. Surveys Tutorials*, vol. 20, no. 4, pp. 2714–2741, Fourth-quarter 2018.

[4] T. Ma, B. Qian, X. Qin, X. Liu, H. Zhou, and L. Zhao, "Satellite-terrestrial integrated 6G: An ultra-dense LEO networking management architecture," *IEEE Wireless Commun.*, vol. 31, no. 1, pp. 62–69, Feb. 2024.

[5] Y. Su, Y. Liu, Y. Zhou, J. Yuan, H. Cao, and J. Shi, "Broadband LEO satellite communications: Architectures and key technologies," *IEEE Wireless Commun.*, vol. 26, no. 2, pp. 55–61, Apr. 2019.

[6] H. D. Le, T. V. Nguyen, and A. T. Pham, "Cloud attenuation statistical model for satellite-based FSO communications," *IEEE Antenna Wireless Propag. Lett.*, vol. 20, no. 5, pp. 643–647, May 2021.

[7] A. Abdi, W. Lau, M.-S. Alouini, and M. Kaveh, "A new simple model for land mobile satellite channels: first- and second-order statistics," *IEEE Trans. Wireless Commun.*, vol. 2, no. 3, pp. 519–528, May 2003.

[8] G. Pan, J. Ye, Y. Zhang, and M.-S. Alouini, "Performance analysis and optimization of cooperative satellite-aerial-terrestrial systems," *IEEE Trans. Wireless Commun.*, vol. 19, no. 10, pp. 6693–6707, Oct. 2020.

[9] K. An, M. Lin, J. Ouyang, and W.-P. Zhu, "Secure transmission in cognitive satellite terrestrial networks," *IEEE J. Sel. Areas Commun.*, vol. 34, no. 11, pp. 3025–3037, Nov. 2016.

[10] J. Ye, G. Pan, and M.-S. Alouini, "Earth rotation-aware non-stationary satellite communication systems: Modeling and analysis," *IEEE Trans. Wireless Commun.*, vol. 20, no. 9, pp. 5942–5956, Sep. 2021.

[11] B. R. Bean and G. D. Thayer, "Models of the atmospheric radio refractive index," *Proc. IRE*, vol. 47, no. 5, pp. 740–755, May 1959.

[12] L. V. Blake, "Ray height computation for a continuous nonlinear atmospheric refractive-index profile," *Radio Science*, vol. 3, no. 1, pp. 85–92, Jan. 1968.

[13] W. D. Hershberger, "The absorption of microwaves by gases," *J. Appl. Phys.*, vol. 17, no. 6, pp. 495–500, Jun. 1946. [Online]. Available: https://doi.org/10.1063/1.1707744

[14] P. W. Rosenkranz, "Absorption of microwaves by atmospheric gases"*, in Atmospheric Remote Sensing by Microwave Radiometry,* M. Janssen, Ed. New York: Wiley, 1993.

[15] L. C. Sutherland and H. E. Bass, "Atmospheric absorption in the atmosphere up to 160 km," *J. Acoust. Soc. Am.*, vol. 115, no. 3, pp. 1012–1032, Feb. 2004. [Online]. Available: https://doi.org/10.1121/1.1631937

[16] J. Kokkoniemi, J. M. Jornet, V. Petrov, Y. Koucheryavy, and M. Juntti, "Channel modeling and performance analysis of airplane-satellite Terahertz band communications," *IEEE Trans. Veh. Technol.*, vol. 70, no. 3, pp. 2047–2061, Mar. 2021.

[17] X. Wang, N. Deng, and H. Wei, "Coverage and rate analysis of LEO satellite-to-airplane communication networks in Terahertz band," *IEEE Trans. Wireless Commun.*, vol. 22, no. 12, pp. 9076–9090, Dec. 2023.

[18] V. Petrov, M. Komarov, D. Moltchanov, J. M. Jornet, and Y. Koucheryavy, "Interference and SINR in millimeter wave and Terahertz communication systems with blocking and directional antennas," *IEEE Trans. Wireless Commun.*, vol. 16, no. 3, pp. 1791–1808, Mar. 2017.

[19] I. Ali, N. Al-Dhahir, and J. Hershey, "Doppler characterization for LEO satellites," *IEEE Trans. Commun.*, vol. 46, no. 3, pp. 309–313, Mar. 1998.

[20] E. Papapetrou and F.-N. Pavlidou, "Analytic study of Doppler-based handover management in LEO satellite systems," *IEEE Trans. Aerosp. Electron. Syst.*, vol. 41, no. 3, pp. 830–839, Jul. 2005.

[21] E. Haas, "Aeronautical channel modeling," *IEEE Trans. Veh. Technol.*, vol. 51, no. 2, pp. 254–264, Mar. 2002.

[22] C. Xu, J. Zhang, T. Bai, P. Botsinis, R. G. Maunder, R. Zhang, and L. Hanzo, "Adaptive coherent/non-coherent single/multiple-antenna aided channel coded ground-to-air aeronautical communication," *IEEE Trans. Commun.*, vol. 67, no. 2, pp. 1099–1116, Feb. 2019.

[23] Q. Zhang, H. Sun, Z. Feng, H. Gao, and W. Li, "Data-aided Doppler frequency shift estimation and compensation for UAVs," *IEEE Internet Things J.*, vol. 7, no. 1, pp. 400–415, Jan. 2020.

[24] V. Khammammetti and S. K. Mohammed, "OTFS-based multiple-access in high Doppler and delay spread wireless channels," *IEEE Wireless Commun. Lett.*, vol. 8, no. 2, pp. 528–531, Apr. 2019.

[25] L. Gaudio, M. Kobayashi, G. Caire, and G. Colavolpe, "On the effectiveness of OTFS for joint radar parameter estimation and communication," *IEEE Trans. Wireless Commun.*, vol. 19, no. 9, pp. 5951–5965, Sep. 2020.

[26] International Telecommunication Union recommendation ITU-R, "Specific attenuation model for rain for use in prediction methods," 2005, P. 838-3. [Online]. Available: https://www.itu.int/dms_pubrec/itu-r/rec/p/R-REC-P.838-3-200503-I!!PDF-E.pdf

[27] S. Zang, M. Ding, D. Smith, P. Tyler, T. Rakotoarivelo, and M. A. Kaafar, "The impact of adverse weather conditions on autonomous vehicles: How rain, snow, fog, and hail affect the performance of a self-driving car," *IEEE Veh. Technol. Mag.,*, vol. 14, no. 2, pp. 103–111, Jun. 2019.

[28] International Telecommunication Union recommendation ITU-R, "Attenuation due to clouds and fog," Feb. 2012, P. 840-5. [Online]. Available: https://www.itu.int/dms_pubrec/itu-r/rec/p/R-REC-P.840-5-201202-S!!PDF-E.pdf

[29] H. D. Le, T. V. Nguyen, and A. T. Pham, "Cloud attenuation statistical model for satellite-based FSO communications," *IEEE Antennas Wireless Propag. Lett.*, vol. 20, no. 5, pp. 643–647, May 2021.

[30] S. Sharma and R. Mishra, "A simulation model for nakagmi-m fading channel with m>1," *Int. J. Adv. Comput. Sci. Appl.*, vol. 6, no. 10, 2015. [Online]. Available: http://dx.doi.org/10.14569/IJACSA.2015.061040

[31] International Telecommunication Union recommendation ITU-R, "The radio refractive index: its formula and refractivity data," pp. 453–459, Jul. 2015. [Online]. Available: https://www.itu.int/dms_pubrec/itu-r/rec/p/R-REC-P.453-11-201507-S!!PDF-E.pdf

[32] C. Xu, T. Bai, J. Zhang, R. Rajashekar, R. G. Maunder, Z. Wang, and L. Hanzo, "Adaptive coherent/non-coherent spatial modulation aided unmanned aircraft systems," *IEEE Wireless Commun.*, vol. 26, no. 4, pp. 170–177, Aug. 2019.

[33] A. Goldsmith and S.-G. Chua, "Variable-rate variable-power MQAM for fading channels," *IEEE Trans. Commun.*, vol. 45, no. 10, pp. 1218–1230, Oct. 1997.

[34] J. Jang and K. B. Lee, "Transmit power adaptation for multiuser OFDM systems," *IEEE J. Sel. Areas Commun.*, vol. 21, no. 2, pp. 171–178, Feb. 2003.

[35] G. J. Foschini and J. Salz, "Digital communications over fading radio channels," *Bell Syst. Tech. J.*, pp. 429–456, Feb. 1983.

[36] T. Wang, J. Proakis, E. Masry, and J. Zeidler, "Performance degradation of OFDM systems due to Doppler spreading," *IEEE Trans. Wireless Commun.*, vol. 5, no. 6, pp. 1422–1432, Jun. 2006.

[37] N. Beaulieu and C. Cheng, "Efficient nakagami-m fading channel simulation," *IEEE Trans. Veh. Commun.*, vol. 54, no. 2, pp. 413–424, Mar. 2005.
[38] U. Silva Dias, M. Daoud Yacoub, J. C. S. Santos Filho, G. Fraidenraich, and D. Benevides da Costa, "On the Nakagami-m autocorrelation and power spectrum functions: Field trials and validation," in *Proc. Int. Telecommun. Symp.*, Sep. 2006, pp. 253–256.
[39] C.-D. Iskander and P. Mathiopoulos, "Analytical envelope correlation and spectrum of maximal-ratio combined fading signals," *IEEE Trans. Veh. Commun.*, vol. 54, no. 1, pp. 399–404, Jan. 2005.
[40] C. Zhang, Y. Liu, W. Yi, Z. Qin, and Z. Ding, "Semi-grant-free NOMA: Ergodic rates analysis with random deployed users," *IEEE Wireless Commun. Lett.*, vol. 10, no. 4, pp. 692–695, Apr. 2021.
[41] B. Zhao, C. Zhang, W. Yi, and Y. Liu, "Ergodic rate analysis of STAR-RIS aided NOMA systems," *IEEE Commun. Lett.*, vol. 26, no. 10, pp. 2297–2301, Oct. 2022.
[42] A. P. Prudniko, Y. A. Brychkov, and O. I. Marichev, *Integrals and Series: Special Functions,* vols 1-2, 1st ed. Boca Raton, FL, USA: CRC Press, Nov. 1986.
[43] "Zenith absorption data," Earth Observation Data Group - University of Oxford, 2025, accessed: Mar. 13, 2025. [Online]. Available: https://eodg.atm.ox.ac.uk/ATLAS/zenith-absorption
[44] C. Xu, L. Xiang, J. An, C. Dong, S. Sugiura, R. G. Maunder, L.-L. Yang, and L. Hanzo, "OTFS-aided RIS-assisted SAGIN systems outperform their OFDM counterparts in doubly selective high-Doppler scenarios," *IEEE Internet of Things Journal*, vol. 10, no. 1, pp. 682–703, Jan. 2023.
[45] I. S. Gradshteyn and I. M. Ryzhik, *Table of Integrals, Series, and Products*, 5th ed. San Diego, CA: Academic, 1994.
[46] C. Zhang, W. Yi, Y. Liu, and L. Hanzo, "Semi-integrated-sensing-and-communication (Semi-ISaC): From OMA to NOMA," *IEEE Trans. Commun.*, vol. 71, no. 4, pp. 1878–1893, Apr. 2023.
[47] Z. Yang, Z. Ding, and P. Fan, "Performance analysis of cloud radio access networks with uniformly distributed base stations," *IEEE Trans. Veh. Technol.*, vol. 65, no. 1, pp. 472–477, Jan. 2016.
[48] M. Kang and M. Alouini, "Capacity of MIMO rician channels," *IEEE Trans. Wireless Commun.*, vol. 5, no. 1, pp. 112–122, Jan. 2006.
[49] G. D. Thayer, "A rapid and accurate ray tracing algorithm for a horizontally stratified atmosphere," *Radio Science*, vol. 2, no. 2, pp. 249–252, 1967. [Online]. Available: https://agupubs.onlinelibrary.wiley.com/doi/abs/10.1002/rds196722249
[50] L. Rayleigh, "On the theory of stellar scintillation," *The London, Edinburgh, and Dublin Philosophical Magazine and Journal of Science*, vol. 36, no. 218, pp. 129–142, 1893. [Online]. Available: https://doi.org/10.1080/14786449308620456
[51] M. Abramowitz and I. A. Stegun, *Handbook of Mathematical Functions With Formulas, Graphs, and Mathematical Tables*, 10th ed. New York, NY, USA: Dover, 1972.